

Chemical Abundances for a Sample of FGK dwarfs in the Pleiades Open Cluster from APOGEE

Vinicius Grilo,^{1*} Diogo Souto,¹ Katia Cunha,^{3,2} Rafael Guerço,^{4,2} Rodrigo Vieira,¹ Verne Smith,⁵ Deusaete Vilar,¹ Anderson Andrade,¹ Fabio Wanderley,² Simone Daflon,² João Victor Sales Silva²

¹*Departamento de Física, Universidade Federal de Sergipe, Av. Marcelo Deda Chagas, S/N, 49107-230 São Cristóvão, SE, Brazil*

²*Observatório Nacional/MCTIC, R. Gen. José Cristino, 77, 20921-400, Rio de Janeiro, Brazil*

³*Steward Observatory, University of Arizona, 933 North Cherry Avenue, Tucson, AZ 85721-0065, USA*

⁴*Instituto de Astronomía, Universidad Católica del Norte, Av. Angamos 0610, Antofagasta, Chile*

⁵*NSF's NOIRLab, 950 N. Cherry Ave. Tucson, AZ 85719 USA*

Accepted XXX. Received YYY; in original form ZZZ

ABSTRACT

This paper presents chemical abundances of twelve elements (C, Na, Mg, Al, Si, K, Ca, Ti, V, Cr, Mn, and Fe) for 80 FGK dwarfs in the Pleiades open cluster, which span a temperature range of ~ 2000 K in T_{eff} , using the high-resolution ($R \sim 22,500$) near-infrared SDSS-IV/APOGEE spectra ($\lambda 1.51\text{--}1.69\ \mu\text{m}$). Using a 1D LTE abundance analysis, we determine an overall metallicity of $[\text{Fe}/\text{H}] = +0.03 \pm 0.04$ dex, with the elemental ratios $[\alpha/\text{Fe}] = +0.01 \pm 0.05$, $[\text{odd-z}/\text{Fe}] = -0.04 \pm 0.08$, and $[\text{iron peak}/\text{Fe}] = -0.02 \pm 0.08$. These abundances for the Pleiades are in line with the abundances of other open clusters at similar galactocentric distances as presented in the literature. Examination of the abundances derived from each individual spectral line revealed that several of the stronger lines displayed trends of decreasing abundance with decreasing T_{eff} . The list of spectral lines that yield abundances that are independent of T_{eff} are presented and used for deriving the final abundances. An investigation into possible causes of the temperature-dependent abundances derived from the stronger lines suggests that the radiative codes and the APOGEE line list we employ may inadequately model van der Waals broadening, in particular in the cooler K dwarfs.

Key words: infrared: stars — open clusters and associations: individual — stars: abundances — stars: fundamental parameters

1 INTRODUCTION

Open clusters are groups of relatively young, gravitationally bound stars that reside across the Milky Way disk. Under the assumption that these open clusters originate from a common progenitor giant molecular cloud (GMC) (Krumholz, McKee & Bland-Hawthorn 2019), a uniform and well-mixed chemical distribution composition is expected to result from a single, simultaneous event of star formation. Consequently, members within these clusters should share not only the same age, galactocentric distance, and initial chemical composition but also differ solely in their initial stellar masses, as indicated by studies such as De Silva et al. (2006, 2007), Feng & Krumholz (2014) and Bovy (2016). This unique scenario makes star clusters one of the most important astrophysical laboratories. They are ideal environments for investigating interactions between stellar chemistry and internal physical processes throughout the stars' evolution, which may contribute to deviations from chemical homogeneity.

The Pleiades open cluster is one of the most extensively studied clusters in the literature, with numerous surveys conducted at various wavelengths to investigate its chemical and dynamic nature (e.g. Gaia (Gaia Collaboration 2018), APOGEE (Apache Point Observatory Galactic Evolution Experiment; Majewski et al. 2017) and GALAH (Galactic Archaeology with HERMES; De Silva et al.

2015). The availability of Gaia DR2 and DR3 data have elucidated the debate regarding the distance to the Pleiades (vanLeeuwen 2009; Abramson 2018), inferring that the cluster is situated at a distance of 135.15 ± 0.43 pc (Lodieu et al. 2019), and thus refuting the previous estimate of 120.2 ± 1.9 pc (vanLeeuwen 2009) derived from Hipparcos data. Although the Pleiades cluster is very close to us, it lies at a position with measurable reddening along the line of sight ($E(B - V) \sim 0.04$ mag; O'Dell, Hendry & Collier Cameron 2014 and Gaia Collaboration 2018).

This cluster consists of young stars with approximately solar metallicity. Some determinations of metallicity include $[\text{Fe}/\text{H}]$ values of: $[\text{Fe}/\text{H}] = -0.034 \pm 0.024$ (Boesgaard & Friel 1990); $+0.06 \pm 0.05$ (King et al. 2000); $+0.06 \pm 0.02$ (Gebran & Monier 2008); $+0.03 \pm 0.05$ (Funayama et al. 2009); and $+0.03 \pm 0.02$ (Soderblom et al. 2009). However, most studies on metallicities and abundances of Pleiades open cluster members focus on solar-like or warmer F-A stars, with a lack of precise abundance analyses in stars covering a wide range of effective temperatures.

The age of the Pleiades open cluster has been debated in the literature often, ranging from 70–130 Myr from determinations using isochrone fitting (Mermilliod 1981; Vandenberg & Bridges 2009; Mazzei & Pigatto 1989; Gossage et al. 2018), while the lithium depletion boundary method (Basri, Marcy & Graham 1996; Stauffer, Schultz & Kirkpatrick 1998; Barrado y Navascués, Stauffer &

* E-mail: vinicius.grilo@academico.ufs.br

Jayawardhana 2004) suggests an age of about 112 ± 5 Myr (Dahm 2015).

One of the processes possible to study in stellar clusters is atomic diffusion, a physical process that operates more efficiently in turnoff stars (Vauclair, Vauclair & Michaud 1978; Choi et al. 2016; Dotter 2016; Dotter et al. 2017). Diffusion signatures have been found in stars belonging to globular clusters (NGC 6397 by Korn et al. 2007, Lind et al. 2008, and Nordlander et al. 2012; NGC 6752 by Gruyters et al. 2013 and Gruyters, Nordlander & Korn 2014; and M30 by Gruyters et al. 2016, Gavel et al. 2021, and Nordlander et al. 2024) and open clusters (M67 by Souto et al. 2018; Gao et al. 2018; Bertelli Motta 2018; Souto et al. 2019, NGC 2420 by Semenova et al. 2020, and Coma Berenices by Souto et al. 2021). Atomic diffusion is a process dependent on age and metallicity (Michaud, Alecian & Richer 2015). The study of the chemical abundances of Pleiades stellar members offers the possibility to put observational limits to the amount of diffusion taking place at those stars with effective temperatures around 6500 K.

The purpose of this work is to determine the stellar chemical abundances of twelve elements (C, Na, Mg, Al, Si, K, Ca, Ti, V, Cr, Mn, and Fe) using high-resolution APOGEE spectra for F, G, and K main-sequence stars from the Pleiades open cluster, spanning a large range in effective temperatures (from $\sim 4500 - 6800$ K). This paper is organized as follows: Section 2 describes the observational data and sample selection; Section 3 details the atmospheric parameters and the methodology used to derive individual abundances; Sections 4 and 5, respectively, present and discuss the main findings; Section 6 offers the concluding remarks of this study.

2 OBSERVATIONS AND SAMPLE

2.1 The APOGEE Spectra

This study is based on data from the SDSS-IV/APOGEE survey. The APOGEE spectrograph was originally commissioned for the Sloan Digital Sky Survey (SDSS) in its third phase (Abazajian et al. 2005), continued to be utilized in the fourth phase (Adelman-McCarthy et al. 2006) and is currently operational in the fifth phase of SDSS (Adelman-McCarthy et al. 2007). The SDSS achieved comprehensive coverage of the sky across both hemispheres, conducting observations at the Las Campanas Observatory (LCO) with the Irénée Du Pont telescope (Bowen & Vaughan 1973) and at the Apache Point Observatory (APO) using the Sloan Foundation Telescope (Gunn et al. 2006). Both facilities employ telescopes with a 2.5-meter diameter, outfitted with the APOGEE-S and APOGEE-N spectrographs, respectively (Wilson et al. 2019).

The APOGEE spectrographs (Wilson et al. 2010) are cryogenic, high-resolution (with a spectral resolution $R = \lambda/\delta\lambda \sim 22,500$) spectrographs operating in the H-band, specifically in the near-infrared spectral region between $1.51 - 1.69 \mu\text{m}$. These instruments are multi-object, comprised of a set of fibers, enabling the simultaneous acquisition of stellar spectra from 300 targets. In the SDSS-V phase, under the Milky Way Mapper survey, the APOGEE spectrographs continue to operate with minor modifications from their SDSS-IV configuration (Kollmeier et al. 2019), although the main goal of the survey is to observe main-sequence stars instead of red-giants.

In this work, we utilize spectra from the final public data release of the SDSS-IV/APOGEE, specifically DR17 (Abdurro'uf 2022). DR17 offers comprehensive coverage of various star clusters (Donor et al. 2020), including the Pleiades open cluster, which is the focus of this research. The spectra were processed using the APOGEE

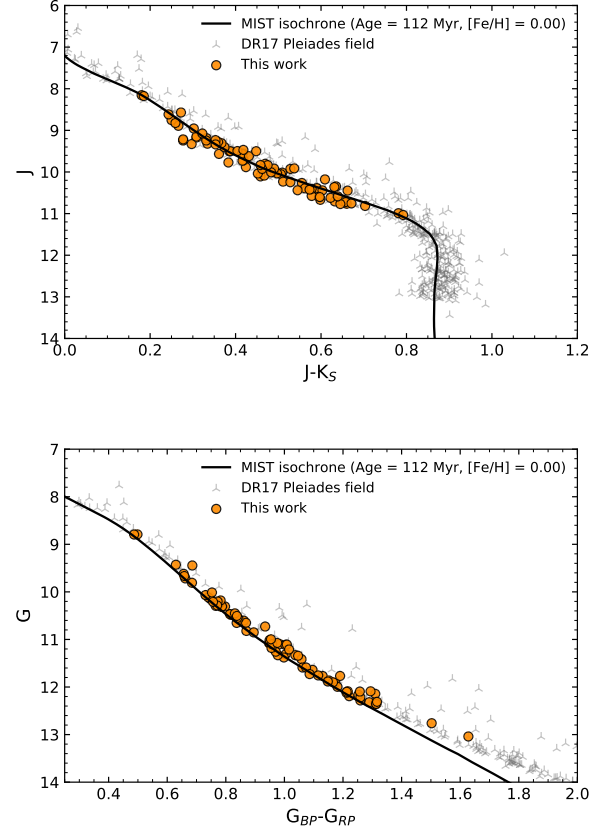


Figure 1. The top and bottom panels show the diagrams ($J-K_S$) vs. J and ($G_{BP}-G_{RP}$) vs. G for the Pleiades field stars observed by APOGEE (gray inverted triangles), using the reddening corrected photometry from 2MASS and Gaia DR3, respectively. The orange circles represent the stars studied in this work. MIST isochrones are also displayed as solid black lines.

pipeline, as detailed in Nidever et al. (2015) with further refinements described in Holtzman et al. (2018) and Jönsson et al. (2020).

2.2 The Sample

We use the work of Lodieu et al. (2019) as a reference for our membership analysis in the Pleiades. Lodieu et al. (2019) provide a revised membership list for three clusters, the Pleiades included, from a five-dimensional analysis ($\alpha, \delta, \pi, \mu_\alpha \cos \delta, \mu_\delta$) using data from the Gaia DR2 catalog (Gaia Collaboration 2018), complemented by comparisons with well known large-scale surveys, such as, the Two Micron All-Sky Survey (2MASS; Cutri et al. 2003; Skrutskie et al. 2006), the Sloan Digital Sky Survey Data Release 12 (SDSS; Abolfathi et al. 2018), the UKIRT Infrared Deep Sky Survey Galactic Clusters Survey (UKIDSS GCS; Lawrence et al. 2007), the Wide-field Infrared Survey Explorer (AllWISE; Wright et al. 2010; Cutri et al. 2014), and the first data release of the Panoramic Survey Telescope and Rapid Response System (PS1; Kaiser et al. 2002; Chambers et al. 2016).

The authors obtained a total of 1248 bona-fide members of the Pleiades cluster with a tidal radius of 11.6 pc. Based on this list, we performed a cross-match with the DR17 APOGEE sample, resulting in 425 stars in common. We then removed 232 M dwarfs with effective temperatures ($T_{\text{eff}} < 4100$ K) from this list because

their spectra present significant molecular absorption (particularly from H_2O), and their study would require an analysis beyond the scope of this work (see discussions in Souto et al. 2020, 2021, 2022; Wanderley et al. 2023). Also, we removed from the sample 33 stars with $T_{\text{eff}} > 7000$ K because most of their atomic lines were too weak to be precisely studied, resulting in a total of 149 stars. We note that we used the APOGEE uncalibrated values for the effective temperature in this selection criteria. A few stars in this sample were flagged in DR17 with warnings such as SUSPECT_BROAD_LINES, SUSPECT_ROTATION, and PERSIST_HIGH. To ensure the quality and reliability of the spectra analyzed, we conducted a detailed visual analysis of each spectrum before analysis.

We then removed stars displaying double lines in their spectra and likely to be spectroscopic binaries, stars that were likely binaries based on their positions on the color-magnitude diagram, and those with radial velocity scatter higher than 1.0 km.s^{-1} (El-Badry et al. 2018). We also removed stars having spectra with signal-to-noise (SNR) < 100 , and those with $v_{\text{sin}(i)} > 30 \text{ km.s}^{-1}$, as rotation velocity contributes to the broadening of absorption lines, making abundance determinations more challenging. Finally, we note that the stars 2M03491172+2438117 and 2M03440424+2459233 have not been removed from the sample, although they exhibit a radial velocity scatter of 17.7 km.s^{-1} (from 2 APOGEE visits) and 2.9 km.s^{-1} (from 3 APOGEE visits), respectively, suggesting that they are likely members of binary systems. However, we chose to retain them in our sample in order to compare abundance results with Spina et al. (2018) (Section 4.1.2). Our final sample contains 86 stars, covering the effective temperature range roughly between 4500 – 6850 K.

A verification of the radial velocities of the stars in this sample indicated that some of them exhibited radial velocities (RV) that significantly deviated from the expected cluster value of $5.54 \pm 0.10 \text{ km.s}^{-1}$ (Gaia Collaboration 2018). These deviations exceeded 3σ of the typical RV uncertainty from APOGEE spectra (1 km.s^{-1}). To refine our membership criteria, we applied the Hierarchical Density-Based Spatial Clustering of Applications with Noise (HDBSCAN; Campello, Moulavi & Sander 2013) algorithm, using radial velocity as a key indicator. This approach was chosen because Lodieu et al. (2019) did not use radial velocity, and it leverages spectroscopic data from the APOGEE spectra. The HDBSCAN is a density-based clustering algorithm commonly used in machine learning and data analysis. It builds upon the Density-Based Spatial Clustering of Applications with Noise (DBSCAN, Ester et al. 1996) algorithm but introduces a hierarchical approach to cluster extraction, having better performances when compared to DBSCAN and to similar methods like Gaussian Mixture models (Hunt & Reffert 2021).

Among the input parameters of the HDBSCAN, the most important are the *minimum number of points* (m_{Pts}) and the *minimum cluster size* (m_{clSize}). The m_{Pts} is analogous to the epsilon parameter in DBSCAN and defines core and border: points with fewer than m_{Pts} neighbors are considered outliers. The m_{clSize} sets the minimum number of points required to form a cluster. We followed the recommendation by Campello, Moulavi & Sander (2013) and considered the same value for both m_{Pts} and m_{clSize} parameters. We assumed $m_{\text{Pts}} = m_{\text{clSize}} = 2$. Keeping the values of m_{Pts} and m_{clSize} as low as possible in HDBSCAN can have several advantages: i) Identifying smaller clusters in the data; ii) m_{Pts} low allows the algorithm to classify more points as outliers, which can be useful for identifying rare or anomalous data points that do not belong to any cluster; iii) More flexibility in capturing diverse structures within the data; and iv) Lowering these parameters can encourage the algorithm to explore different density levels in the data, potentially revealing

hierarchical structures or nested clusters that might be missed with higher parameter values.

We ran the HDBSCAN in our sample of 86 stars, assuming the stellar spectroscopic radial velocity from DR17 and proper motions ($\mu_{\alpha} \cos \delta$, μ_{δ}) from Gaia DR3 (Gaia Collaboration et al. 2021). We confirmed 80 stars belonging to the Pleiades, which composes our final sample shown in Table 1.

In Figure 1, we present color-magnitude diagrams (CMDs) using dereddened data from 2MASS (Skrutskie et al. 2006) ($J-K_S - J$) and Gaia DR3 ($G_{BP} - G_{RP} - G$). The selected targets are displayed as orange circles, while the sample of APOGEE targets observed in the Pleiades field are shown as gray inverted triangles. For comparison, we also display a MIST isochrone (Choi et al. 2016; Dotter 2016) with an age of 112 Myr and solar metallicity as a solid black line, corresponding to the age and metallicity of the Pleiades (Dahm 2015). All magnitudes underwent correction for extinction, employing the mean Pleiades extinction value of $A_V = 0.12$ (Stauffer et al. 2007) and the relationships provided by Wang & Chen (2019). The selected stars from the Pleiades (orange circles) are unevolved, i.e., they have not yet reached the turnoff point, where stars begin their rapid hydrogen exhaustion phase. The points representing the sample and the displayed MIST isochrone agree well.

3 CHEMICAL ABUNDANCE ANALYSIS

3.1 Atmospheric Parameters

The effective temperature values adopted in this study were obtained from APOGEE DR17. We used the raw values from ASPCAP (APOGEE Stellar Parameters and Chemical Abundances Pipeline; García Pérez et al. 2016), a pipeline developed by the APOGEE team for determining stellar parameters (T_{eff} , $\log g$, $[\text{M}/\text{H}]$, $[\text{C}/\text{M}]$, $[\text{N}/\text{M}]$, $[\alpha/\text{H}]$, ξ) and chemical abundances for over 24 elements in all stars observed by APOGEE. ASPCAP uses the FERRE code (Allende Prieto et al. 2006, 2014), and it compares the spectra observed by APOGEE to a library of synthetic spectra using chi-square minimization (χ^2) and identifies the set of stellar parameters and abundances that provide the best fit to the synthetic spectrum.

The surface gravities ($\log g$) for the stars were calculated using the Stefan-Boltzmann equation, expressed as follows:

$$\log g = \log g_{\odot} + \log \left(\frac{M_{\star}}{M_{\odot}} \right) + 4 \log \left(\frac{T_{\text{eff},\star}}{T_{\odot}} \right) - \frac{L_{\text{bol},\star}}{L_{\text{bol},\odot}} \quad (1)$$

Information on stellar mass and luminosity was derived through interpolation of a 125 million-year-old isochrone with a metallicity of $[\text{Fe}/\text{H}] = 0.00$ dex, representative of the Pleiades cluster, from the MESA Isochrones and Stellar Tracks (MIST; Choi et al. 2016; Dotter 2016). The solar reference values used were $T_{\text{eff},\odot} = 5772$ K, $\log g_{\odot} = 4.438$ dex, and bolometric magnitude $M_{\text{bol},\odot} = 4.75$, as recommended by the IAU (Prša et al. 2016).

Table 1: Atmospheric Parameters

2MASS ID	J	H	K	pm ra (mas yr ⁻¹)	pm dec (mas yr ⁻¹)	RV (km s ⁻¹)	SNR	vsini (km s ⁻¹)	T _{eff} (K)	logg (cm s ⁻²)	ξ (km s ⁻¹)
2M03450528+2342097	8.205	8.041	8.000	19.75 ± 0.02	-46.40 ± 0.02	6.2	641	21.0 ± 1.2	6848	4.33	1.6
2M03445123+2316082	8.184	8.006	7.984	20.55 ± 0.02	-44.30 ± 0.02	7.1	617	26.5 ± 1.9	6678	4.35	1.6
2M03435880+2352578 ^a	8.600	8.420	8.308	19.88 ± 0.06	-44.69 ± 0.05	6.0	527	14.6 ± 0.9	6577	4.37	1.6
2M03501766+2522464	8.645	8.469	8.382	19.35 ± 0.03	-45.86 ± 0.02	6.5	684	24.5 ± 1.0	6451	4.39	1.6
2M03475252+2356286	8.853	8.639	8.574	19.68 ± 0.03	-46.39 ± 0.02	6.7	486	20.1 ± 0.0	6251	4.43	1.6
2M03482616+2402544 ^b	8.985	8.719	8.663	19.67 ± 0.02	-46.26 ± 0.01	6.5	306	16.2 ± 1.0	6206	4.44	1.6
2M03444075+2449067	8.783	8.540	8.513	20.24 ± 0.03	-45.45 ± 0.02	4.7	581	19.4 ± 0.8	6169	4.45	1.6
2M03394117+2317271	8.920	8.686	8.634	21.29 ± 0.02	-43.71 ± 0.01	6.3	469	28.4 ± 1.4	6159	4.45	1.6
2M03463878+2457346	9.105	8.851	8.763	20.61 ± 0.02	-46.95 ± 0.01	6.4	574	21.0 ± 0.8	6095	4.46	1.6
2M03491172+2438117 ^{a,b}	9.246	9.028	8.949	20.68 ± 0.03	-44.74 ± 0.02	3.9	273	12.5 ± 0.9	6055	4.47	1.6
2M03504007+2355590	9.181	8.941	8.853	18.71 ± 0.03	-44.36 ± 0.02	6.7	559	24.6 ± 0.9	6030	4.48	1.6
2M03385686+2434112 ^a	9.358	9.053	9.041	20.16 ± 0.02	-43.46 ± 0.02	5.9	530	11.2 ± 0.8	6029	4.48	1.6
2M03462267+2434126 ^b	9.274	8.994	8.923	19.68 ± 0.02	-44.99 ± 0.01	6.9	583	12.7 ± 0.7	6024	4.48	1.6
2M03445639+2425574 ^b	9.218	8.945	8.866	19.70 ± 0.03	-46.14 ± 0.02	5.3	587	18.6 ± 0.7	6020	4.48	1.6
2M03462735+2508080 ^b	9.366	9.063	8.993	20.87 ± 0.02	-45.54 ± 0.02	6.6	497	12.5 ± 0.6	6006	4.48	1.6
2M03483451+2326053 ^b	9.197	8.980	8.868	19.37 ± 0.02	-45.08 ± 0.01	6.4	478	15.4 ± 0.8	5979	4.49	1.6
2M03481712+2353253 ^b	9.264	8.976	8.891	17.89 ± 0.02	-45.50 ± 0.01	6.2	284	14.1 ± 1.0	5966	4.49	1.6
2M03464706+2254525 ^b	9.307	9.032	8.928	18.76 ± 0.02	-45.00 ± 0.02	6.8	470	17.3 ± 0.8	5897	4.50	1.2
2M03465491+2447468 ^{a,b}	9.274	9.005	8.977	19.30 ± 0.02	-46.34 ± 0.01	6.0	483	8.7 ± 0.5	5869	4.51	1.2
2M03465373+2335009 ^b	9.350	9.092	8.996	20.80 ± 0.02	-45.15 ± 0.01	6.6	389	8.7 ± 0.6	5857	4.51	1.2
2M03441391+2446457	9.530	9.172	9.062	20.64 ± 0.02	-45.24 ± 0.01	6.5	432	8.9 ± 0.7	5842	4.51	1.2
2M03474044+2421525 ^b	9.340	9.071	8.953	19.32 ± 0.03	-45.46 ± 0.02	5.5	538	15.9 ± 0.7	5800	4.52	1.2
2M03450400+2515282 ^{a,b}	9.435	9.146	9.041	18.65 ± 0.02	-45.41 ± 0.02	5.4	441	12.6 ± 0.7	5796	4.52	1.2
2M03440424+2459233 ^a	9.499	9.168	9.061	18.69 ± 0.23	-47.79 ± 0.13	5.3	536	8.9 ± 0.7	5755	4.53	1.2
2M03440059+2332382	9.650	9.274	9.199	19.56 ± 0.02	-44.75 ± 0.01	7.4	333	12.7 ± 0.6	5706	4.54	1.2
2M03433195+2340266	9.527	9.192	9.103	19.92 ± 0.07	-45.32 ± 0.05	5.5	323	12.0 ± 0.8	5688	4.54	1.2
2M03493312+2347435	9.595	9.294	9.214	19.92 ± 0.02	-43.75 ± 0.01	7.3	396	6.4 ± 0.7	5688	4.54	1.2
2M03405042+2325064	9.531	9.192	9.123	21.70 ± 0.02	-45.50 ± 0.01	5.8	386	11.7 ± 0.7	5656	4.55	1.2
2M03433772+2332096	9.529	9.191	9.124	19.53 ± 0.02	-45.29 ± 0.01	6.4	433	12.3 ± 0.5	5641	4.55	1.2
2M03481769+2502523	9.593	9.256	9.158	19.52 ± 0.02	-47.06 ± 0.02	6.3	479	12.2 ± 0.6	5577	4.56	1.2
2M03403436+2340574	9.585	9.241	9.148	20.55 ± 0.02	-45.63 ± 0.01	5.7	347	10.8 ± 0.7	5566	4.56	1.2
2M03474811+2313053	9.760	9.436	9.324	20.05 ± 0.03	-45.85 ± 0.02	7.6	416	4.8 ± 1.0	5506	4.57	1.2
2M03502089+2428003	9.746	9.397	9.307	20.35 ± 0.03	-45.48 ± 0.02	5.6	455	8.7 ± 0.6	5501	4.57	1.0
2M03454184+2425534	9.801	9.528	9.398	20.51 ± 0.03	-44.71 ± 0.02	7.3	350	7.1 ± 0.8	5471	4.57	1.0
2M03502130+2305470	9.863	9.512	9.385	19.61 ± 0.03	-46.56 ± 0.02	7.4	393	6.8 ± 0.8	5406	4.58	1.0
2M03444398+2413523	9.913	9.566	9.469	21.47 ± 0.03	-46.45 ± 0.02	5.5	412	9.1 ± 0.8	5370	4.59	1.0
2M03392780+2353420	9.957	9.556	9.475	21.16 ± 0.03	-45.35 ± 0.02	5.0	300	5.5 ± 1.1	5368	4.59	1.0
2M03433440+245429	9.865	9.476	9.370	22.97 ± 0.04	-47.12 ± 0.03	5.3	334	6.3 ± 1.0	5360	4.59	1.0
2M03435070+2414508	9.833	9.429	9.344	21.61 ± 0.03	-44.80 ± 0.02	6.4	413	10.7 ± 0.6	5323	4.59	1.0
2M03470141+2329419	10.037	9.637	9.534	19.07 ± 0.02	-45.02 ± 0.02	6.3	248	8.2 ± 0.9	5271	4.60	1.0
2M03492873+2342440	9.914	9.543	9.428	19.94 ± 0.03	-47.45 ± 0.02	6.1	402	8.2 ± 0.6	5270	4.60	1.0
2M03495035+2342202	10.067	9.699	9.595	19.59 ± 0.03	-44.02 ± 0.02	7.1	346	6.0 ± 0.9	5264	4.60	1.0
2M03505508+2411508	10.116	9.740	9.629	18.86 ± 0.02	-43.39 ± 0.02	6.2	393	9.0 ± 0.8	5216	4.60	1.0
2M03532369+2403542	9.949	9.564	9.439	19.43 ± 0.03	-45.30 ± 0.02	6.9	216	13.7 ± 1.1	5183	4.61	1.0
2M03490232+2315088	10.135	9.758	9.657	19.73 ± 0.02	-44.43 ± 0.02	6.1	304	6.8 ± 1.0	5159	4.61	1.0
2M03461174+2437203	10.062	9.629	9.545	21.20 ± 0.03	-44.70 ± 0.02	6.9	397	8.3 ± 0.8	5106	4.61	1.0
2M03444317+2552319	10.031	9.669	9.520	19.77 ± 0.03	-45.90 ± 0.02	4.1	328	6.2 ± 0.9	5103	4.61	1.0
2M03440484+2416318	9.943	9.494	9.386	20.13 ± 0.02	-45.36 ± 0.02	5.3	205	10.8 ± 0.9	5095	4.61	1.0
2M03573331+2403114	10.454	9.965	9.861	18.76 ± 0.02	-45.31 ± 0.01	6.3	253	2.9 ± 1.4	5016	4.62	1.0
2M03430293+2440110	10.275	9.808	9.727	19.45 ± 0.02	-46.25 ± 0.01	5.6	366	8.2 ± 0.7	5015	4.62	1.0
2M03450326+2350219	10.261	9.835	9.730	20.34 ± 0.02	-45.77 ± 0.01	4.5	158	6.5 ± 1.4	5008	4.62	1.0
2M03513903+2245010	10.435	10.013	9.837	19.60 ± 0.02	-45.60 ± 0.01	6.8	287	3.4 ± 1.3	4997	4.62	1.0
2M03363030+2400440	10.468	10.026	9.903	19.76 ± 0.02	-43.17 ± 0.01	6.0	237	4.4 ± 1.5	4936	4.63	1.0
2M03403072+2429143	10.082	9.659	9.556	21.82 ± 0.04	-44.17 ± 0.03	4.0	332	6.6 ± 1.2	4914	4.63	1.0
2M03444394+2529574	10.391	9.863	9.740	20.32 ± 0.02	-43.83 ± 0.01	5.9	276	7.8 ± 1.0	4906	4.63	1.0
2M03470678+2342546	10.421	9.995	9.839	19.43 ± 0.02	-44.41 ± 0.01	6.6	149	3.3 ± 1.5	4826	4.64	1.0
2M03471480+2522186	10.046	9.515	9.517	19.56 ± 0.02	-45.94 ± 0.02	5.4	364	10.4 ± 0.7	4813	4.64	1.0
2M03434901+2543466	10.294	9.834	9.719	21.27 ± 0.02	-47.77 ± 0.01	5.2	309	10.0 ± 0.9	4800	4.64	1.0
2M03511685+2349357	10.616	10.077	9.957	19.84 ± 0.02	-46.76 ± 0.01	6.5	99	6.7 ± 2.2	4777	4.64	1.0
2M03441120+2322455	9.956	9.512	9.408	22.04 ± 0.03	-46.64 ± 0.02	6.8	374	18.2 ± 0.7	4774	4.64	1.0
2M03505143+2319447	10.632	10.108	10.015	18.89 ± 0.02	-46.33 ± 0.01	7.1	129	4.7 ± 1.9	4736	4.65	1.0
2M03452219+2328182	10.471	9.959	9.848	20.22 ± 0.02	-44.65 ± 0.01	5.9	167	7.9 ± 1.2	4733	4.65	1.0
2M03404256+2542197	10.799	10.240	10.134	20.79 ± 0.02	-45.87 ± 0.01	5.0	262	8.0 ± 1.1	4667	4.65	1.0
2M03440509+2529017	10.605	10.087	10.007	20.77 ± 0.02	-45.66 ± 0.01	5.3	301	8.0 ± 1.0	4667	4.65	1.0
2M03471352+2342515	10.624	10.148	10.009	19.73 ± 0.02	-45.61 ± 0.01	6.6	156	6.2 ± 1.4	4638	4.65	1.0
2M03463938+2401468	10.454	9.986	9.859	20.27 ± 0.02	-46.23 ± 0.01	5.9	171	8.2 ± 1.1	4634	4.65	1.0
2M03420470+2553091	10.784	10.183	10.093	21.06 ± 0.02	-46.90 ± 0.01	4.7	256	9.6 ± 0.9	4623	4.65	1.0
2M03555603+2334021	10.651	10.119	10.009	19.14 ± 0.02	-46.08 ± 0.01	7.2	226	8.7 ± 0.9	4610	4.66	1.0
2M03415906+2555153	10.752	10.167	10.074	20.58 ± 0.02	-45.14 ± 0.01	5.4	252	7.6 ± 1.3	4602	4.66	1.0
2M03422759+2502492	10.736	10.200	10.065	19.37 ± 0.02	-43.27 ± 0.01	5.9	308	8.6 ± 0.7	4599	4.66	1.0
2M03460649+2434027	10.793	10.236	10.113	19.75 ± 0.02	-46.62 ± 0.01	5.5	271	8.3 ± 0.8	4598	4.66	1.0
2M03503457+2430281	10.698	10.197	10.080	19.84 ± 0.02	-45.04 ± 0.02	6.4	307	10.7 ± 0.8	4571	4.66	1.0
2M03401202+2538321	10.208	9.757	9.579	18.35 ± 0.04	-47.55 ± 0.03	3.8	363	15.0 ± 0.8	4570	4.66	1.0
2M03513927+2432561	10.418	9.921	9.808	21.23 ± 0.02	-46.06 ± 0.01	6.4	174	10.4 ± 1.0	4552	4.66	1.0
2M03540892+2420011	10.376	9.845	9.721	16.63 ± 0.03	-46.42 ± 0.02	7.5	323	6.3 ± 1.3	4536	4.66	1.0
2M03413245+2309422	10.845	10.255	10.122	21.49 ± 0.03	-46.00 ± 0.02	5.4	93	6.6 ± 2.1	4531	4.66	1.0
2M03452957+2345379	11.063	10.417	10.251	19.07 ± 0.02	-45.76 ± 0.01	6.3	254	6.3 ± 1.3	4525	4.66	1.0
2M03405126+2335543	10.735	10.209	10.083	21.13 ± 0.02	-45.76 ± 0.01	5.7	124	8.1 ± 1.7	4521	4.66	1.0
2M03432662+2459395	10.477	9.956	9.795	19.04 ± 0.05	-44.59 ± 0.03	5.6	294	9.9 ± 0.9	4514	4.66	1.0
2M03455048+2352262	11.020	10.382	10.219	19.88 ± 0.02	-44.65 ± 0.01	5.0	217	7.6 ± 1.2	4502	4.66	1.0

^a Stars studied by [Spina et al. \(2018\)](#).^b Stars studied by [Soderblom et al. \(2009\)](#).

The microturbulence velocity (ξ) was derived following the same procedure as described by [Smith et al. \(2013\)](#) (see also [Souto et al. 2016](#)). It consists of varying the ξ from 0.5 to 3.0 in steps of 0.5 km.s^{-1} . We adopted the value that results in the lowest dispersion in the abundances of Fe I lines as the microturbulence velocity for the star.

3.2 Metallicities and $v \sin(i)$ determinations using MCMC

We computed spectral syntheses using the radiative transfer code TurboSpectrum ([Alvarez & Plez 1998](#); [Plez et al. 2012](#)) and one-dimensional (1-D) local thermodynamic equilibrium (LTE) and plane-parallel atmospheric models interpolated from the MARCS grid ([Gustafsson et al. 2008](#)). The synthesis uses the APOGEE spectral line list for the H-band ($\lambda = 15,000\text{--}17,000 \text{ \AA}$), which was incorporated into SDSS-V DR16 as outlined by [Smith et al. \(2021\)](#). This line list includes critical transitions for analyzing our sample spectra.

The first step in this analysis was to use the Markov chain Monte Carlo (MCMC) technique to analyze a selection of Fe I lines in the APOGEE spectra, employing a two-dimensional grid of synthetic spectra. The key parameters in our analysis were the iron abundance ($A(\text{Fe})$) and the projected rotational velocity ($v \sin(i)$). To build this synthetic grid, we maintained fixed values for each target's effective temperature, surface gravity, and microturbulence, as specified in Table 1. The grid varies $A(\text{Fe})$ from 6.90 to 7.70 in 0.01 dex increments and $v \sin(i)$ from 1.0 to 40.0 km.s^{-1} in 1 km.s^{-1} steps.

For each star, we generated a comprehensive grid comprising 1640 spectral syntheses. To correct the fiber-to-fiber and wavelength-dependent line spread function (LSF) variations exhibited in APOGEE spectra, we convolved the synthetic spectra with the LSF to match the APOGEE resolution ([Nidever et al. 2015](#); [Wilson et al. 2019](#)).

We calculated chi-squared values for each spectral line considering line center adjustments of $\pm 5 \text{ \AA}$ around all well-defined Fe I lines within the APOGEE spectral range. Our line selection is based on the criteria described in [Souto et al. \(2018\)](#), with exclusions made for weak lines or those impacted by spectral reduction issues.

The posterior probability of the parameters was sampled using `emcee`¹ ([Foreman-Mackey et al. 2013](#)), a Python implementation of the Affine Invariant MCMC Ensemble sampler ([Goodman & Weare 2010](#)). We adopted a likelihood function proportional to $\exp(-\chi_{\text{tot}}^2/2)$, where χ_{tot}^2 corresponds to the sum of the individual line χ^2 's. For intermediate grid values tested during the `emcee` sampling, we interpolated the χ_{tot} values using `griddata` routine, from Python `Scipy`². For each simulation, we used 50 walkers (random-walk samplers) with 50 steps in the initial phase (burn-in) and 100 steps in the final sampling phase (starting from the last state of the burn-in chain). These values were selected because a convergence plateau (seeing a trace plot) for both $A(\text{Fe})$ and $v \sin(i)$ is observed between 50 and 100 steps in the analysis.

3.3 Abundance determinations using BACCHUS

Abundances of C, Na, Mg, Al, Si, K, Ca, Ti, V, Cr, Mn, and Fe were calculated using the BACCHUS wrapper ([Masseron, Merle & Hawkins 2016](#)), in semi-automatic mode, which employs the radiative transfer code TurboSpectrum ([Alvarez & Plez 1998](#); [Plez et](#)

[al. 2012](#)) to generate spectral syntheses that are directly compared to the observed stellar spectra. We convolved the synthetic spectra assuming the APOGEE resolution and the derived $v \sin(i)$ values, and we determined the best-fit syntheses from varying the elemental abundances and using the BACCHUS code to perform chi-squared minimizations between observed and model spectra. The best fits obtained were then confirmed from a visual inspection to verify the quality of the fits.

3.4 Excluding spectral lines with spurious trends

To avoid inconsistent abundance results, we excluded those lines whose abundances exhibited strong correlations with T_{eff} . From an initial list of atomic lines presented in [Souto et al. \(2018\)](#), we removed two C I lines ($\lambda 15784.7 \text{ \AA}$, $\lambda 16005 \text{ \AA}$), three Mg I lines ($\lambda 15740.716 \text{ \AA}$, $\lambda 15748.988 \text{ \AA}$, and $\lambda 15765.842 \text{ \AA}$), two Al I lines ($\lambda 16718.957 \text{ \AA}$, and $\lambda 16750.564 \text{ \AA}$), four Si I lines ($\lambda 15888.410 \text{ \AA}$, $\lambda 15960.063 \text{ \AA}$, $\lambda 16060.009 \text{ \AA}$, and $\lambda 16094.787 \text{ \AA}$), three Ti I lines ($\lambda 15334.847 \text{ \AA}$, $\lambda 15543.756 \text{ \AA}$, and $\lambda 15715.573 \text{ \AA}$), one Mn I line, $\lambda 15217.0 \text{ \AA}$, and 25 Fe I lines. K and Ca display a small abundance trend as a function of T_{eff} for all lines analyzed, but given that the effects are small, the K I and Ca I lines were kept in the analysis. In Table A1, we provide a comprehensive list of spectral lines adopted and removed from this work.

3.5 Abundance uncertainties

Uncertainties in the derived abundances can be estimated from the abundance sensitivities to errors in the atmospheric parameters (such as T_{eff} , $\log g$, and microturbulence), signal-to-noise ratio, and pseudo-continuum normalization ([Jofré et al. 2019](#)). We used the abundance sensitivities from Table 4 of [Souto et al. \(2018\)](#) to assess the uncertainties in our derived abundances. This error analysis consisted of changing/perturbing the atmospheric parameters based on their typical uncertainties: $\delta T_{\text{eff}} \pm 50 \text{ K}$, $\delta \log g \pm 0.20 \text{ dex}$, $\delta [\text{Fe}/\text{H}] \pm 0.20 \text{ dex}$, and $\delta \xi \pm 0.20 \text{ km.s}^{-1}$. We also accounted for uncertainties stemming from changes in the signal-to-noise ratio and pseudo-continuum normalization, using the same methodology as in [Melo et al. \(2024\)](#). To assess the impact of the SNR on our results, we introduced a controlled amount of noise into our synthetic spectra, varying the SNR from 100 to 300 in increments of 20. We then derived the abundances from these spectra to evaluate how each elemental abundance was affected by changes in SNR. For the pseudo-continuum normalization, we adjusted the spectra by $\pm 0.5\%$ and recalculated the abundances to determine the impact on each element. This analysis was conducted using three representative models for the F-dwarfs ($T_{\text{eff}} = 6400 \text{ K}$, $\log g = 4.30$), G-dwarfs ($T_{\text{eff}} = 5777 \text{ K}$, $\log g = 4.44$), and K-dwarfs ($T_{\text{eff}} = 4800 \text{ K}$, $\log g = 4.60$).

Finally, we combined all uncertainties, from atmospheric parameters, signal-to-noise ratio, and pseudo-continuum normalization, by summing the respective errors in quadrature. The abundance uncertainties for all elements are presented at the bottom of Table 3. The abundance uncertainty obtained for Fe is 0.06 dex, which is similar to the typical abundance uncertainties for all elements. Potassium abundances have the smallest uncertainties ($\sim 0.04 \text{ dex}$), while the abundances of magnesium and aluminum have the largest uncertainties of 0.10 and 0.08 dex, respectively. Another proxy for abundance uncertainties is the standard deviation of the mean. The star-to-star abundance deviation for all elements studied in this work (see Table 3) is about 0.06, in general agreement with the propagated uncertainties obtained.

¹ Available online under the MIT License: <https://github.com/dfm/emcee>.

² For more details on the SCIPY package, refer to [Virtanen et al. \(2020\)](#).

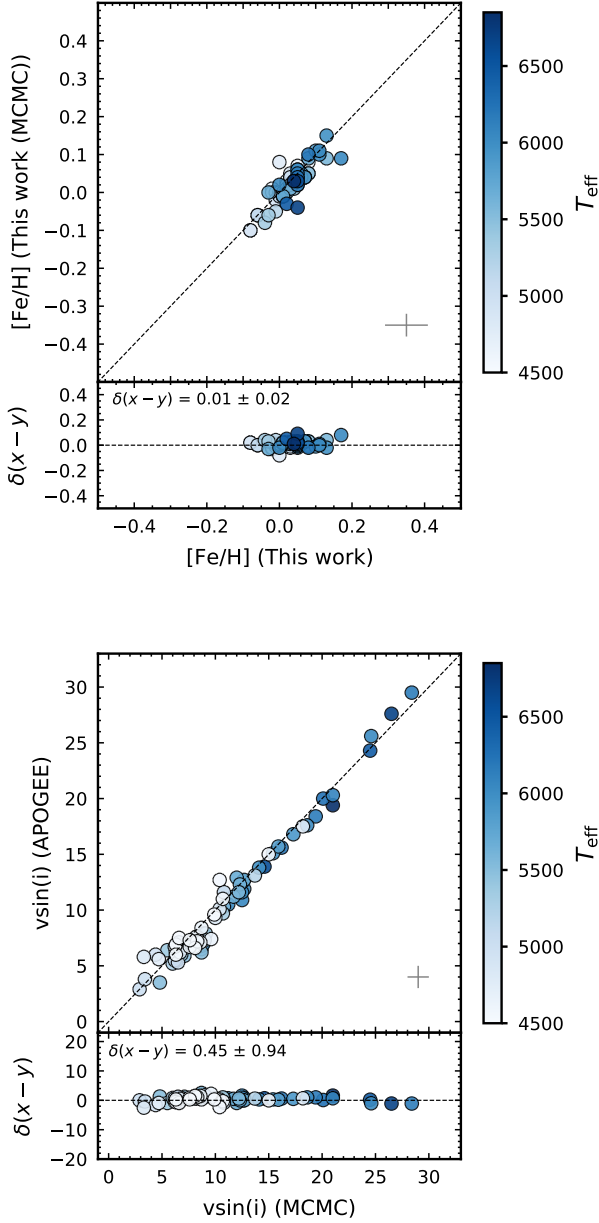


Figure 2. Upper panel: The $[\text{Fe}/\text{H}]$ vs. $[\text{Fe}/\text{H}]$ distribution with this work’s results from the semi-automatic BACCHUS abundance analysis on the x-axis and from MCMC on the y-axis. The subpanel shows the residual (x–y) diagram, where a mean value difference with the respective standard deviation of the mean is defined as δ . A color bar is used to represent the effective temperatures of the stars. Lower panel: same format as the upper panel, but comparing $\text{vsin}(i)$ values measured by our MCMC analysis on the x-axis and from APOGEE on the y-axis. A typical error bar is presented at the bottom right of the figure.

As discussed in Section 3.2, an MCMC analysis of the sample Fe I lines was used as an additional method to determine the stellar metallicities in this study. The MCMC methodology can provide an independent assessment of the uncertainties in the abundance measurements, as it directly estimates the uncertainties in the parameters by means of the standard deviations of the marginalized posteriors. In our case, the mean uncertainties obtained from MCMC for $[\text{Fe}/\text{H}]$

Table 2. Non-LTE abundance corrections.

Element	$T_{\text{eff}} = 4800\text{K}$ $\log g = 4.60$	$T_{\text{eff}} = 5777\text{K}$ $\log g = 4.44$	$T_{\text{eff}} = 6400\text{K}$ $\log g = 4.30$
Fe	0.00	0.00	0.00
Mg	0.00	0.01	0.02
Si	0.00	0.00	-0.01
Mn	0.06	0.12	0.16

was ± 0.06 dex (internal uncertainties + typical standard deviation of the mean), and this is the same as the total uncertainties for iron abundances in Table 3, confirming that the estimated uncertainties using the abundance sensitivities to errors in parameters are probably good estimates of the uncertainties in the derived abundances.

3.6 Non-LTE corrections

Departures from local thermodynamic equilibrium (non-LTE) are important to consider and, in particular, significantly impact the optical spectra of evolved metal-poor stars (Asplund 2005). However, in the near-infrared regime, these effects are generally less pronounced for main-sequence FGK dwarfs (Bergemann et al. 2012; Osorio et al. 2020). The study of Osorio et al. (2020) provides a detailed analysis of multi-element non-LTE calculations for Na, Mg, K, and Ca, crucial for understanding the influence of atomic interactions on stellar abundance determinations in late-type stars. These model grids were essential for developing the synthetic spectra grids utilized in the APOGEE survey’s DR17 ASPCAP results. Osorio et al. (2020) discuss that while non-LTE corrections were modest in the H-band (< 0.10 for all studied species), in the optical range, they reached up to 0.7 dex, underscoring the necessity of non-LTE considerations in stellar spectroscopy to achieve accuracies better than 10%.

We also investigated departures from local thermodynamical equilibrium in our derived abundances for each spectral line studied, applying non-LTE corrections based on Bergemann & Gehren (2008) and the series of studies by Bergemann et al. (2012, 2013, 2015), which can be accessed from nlte.mpia.de. These corrections utilized 1-D plane-parallel models for representative stars in this study. We found that non-LTE deviations for Fe, Mg, and Si are negligible and typically smaller than 0.02 dex for each analyzed line. See Table 2. Manganese showed more significant non-LTE departures across all T_{eff} ranges, varying between +0.06 and +0.16 dex, with a mean correction of +0.12 dex. Since the non-LTE corrections are insignificant, we use our derived LTE abundances in all subsequent discussions in this paper, except for the manganese abundances discussed in Section 4, which were corrected for non-LTE.

Table 3: Derived Stellar Abundances

2MASS ID	[Fe/H] (MCMC)	[Fe/H]	[C/H]	[Na/H]	[Mg/H]	[Al/H]	[Si/H]	[K/H]	[Ca/H]	[Ti/H]	[V/H]	[Cr/H]	[Mn/H]
2M03450528+2342097	0.03 ± 0.02	0.04	-0.10	...	0.04	-0.08
2M03445123+2316082	-0.04 ± 0.02	0.05	0.13	...	-0.01
2M03435880+2352578	0.03 ± 0.03	0.05	-0.11	0.01	0.04	-0.04	0.12	-0.32
2M03501766+2522464	-0.03 ± 0.02	0.02	0.01	0.02	-0.23
2M03475252+2356286	0.04 ± 0.03	-0.03	-0.10	-0.02	0.02	0.03	0.09	-0.24
2M03482616+2402544	0.10 ± 0.02	0.05	-0.14	0.00	0.09	0.00	0.16	-0.09
2M03444075+2449067	0.05 ± 0.02	0.08	-0.01	0.00	0.00	-0.05	0.15	-0.11
2M03394117+2317271	0.02 ± 0.02	0.05	0.09	0.01	0.04	-0.03	0.09	-0.13
2M03463878+2457346	0.04 ± 0.02	0.05	0.04	...	0.12	-0.05
2M03491172+2438117	0.03 ± 0.01	0.05	-0.08	...	-0.04	0.04	-0.03	-0.09	0.13	0.14	-0.13
2M03504007+2355590	0.02 ± 0.02	0.00	...	0.14	-0.05	0.01	0.02	-0.04	0.06	-0.18
2M03385686+2434112	0.09 ± 0.02	0.17	...	0.20	-0.16	0.08	0.08	-0.01	0.17	0.03
2M03462267+2434126	0.11 ± 0.02	0.11	-0.08	0.11	-0.06	0.06	0.08	0.04	-0.08
2M03445639+2425574	0.06 ± 0.02	0.05	-0.09	0.04	-0.04	0.09	0.04	0.04	0.13	-0.18
2M03462735+2508080	0.10 ± 0.02	0.11	...	0.14	-0.08	0.08	0.09	0.07	0.17	-0.03
2M03483451+2326053	0.04 ± 0.02	0.05	...	0.10	-0.04	0.05	0.02	-0.04	0.07	0.18	-0.22
2M03481712+2353253	0.15 ± 0.02	0.13	...	0.13	-0.08	0.08	0.11	0.09	0.18	0.19	0.01
2M03464706+2254525	0.04 ± 0.02	0.07	...	0.14	0.02	0.12	0.07	-0.12	0.13	0.17	-0.18
2M03465491+2447468	0.04 ± 0.02	0.06	...	0.07	-0.01	0.01	0.01	-0.01	0.14	0.12	-0.19
2M03465373+2335009	0.06 ± 0.02	0.05	...	0.09	0.03	0.05	0.04	-0.03	0.15	0.11	-0.24
2M03441391+2446457	0.04 ± 0.02	0.07	...	0.10	0.03	0.00	0.03	-0.11	0.15	0.14	-0.09
2M03474044+2421525	0.11 ± 0.03	0.10	...	0.07	-0.03	0.18	0.10	-0.02	0.18	0.21	-0.15
2M03450400+2515282	0.05 ± 0.02	0.04	...	0.08	0.03	0.17	0.04	0.07	0.12	0.20	-0.14
2M03440424+2459233	-0.01 ± 0.02	0.02	...	0.02	-0.01	-0.01	-0.04	-0.04	0.12	0.08	-0.18
2M03440059+2332382	0.04 ± 0.02	0.07	...	0.05	-0.04	0.07	0.08	-0.07	0.13	-0.16
2M03493312+2347435	0.09 ± 0.02	0.08	0.02	0.05	0.06	0.07	0.19	0.10	-0.11
2M03433195+2340266	0.00 ± 0.02	-0.03	0.02	0.01	-0.06	0.07	-0.30
2M03405042+2325064	0.01 ± 0.02	0.03	...	0.09	0.00	-0.04	0.03	-0.05	0.11	-0.03	-0.15
2M03433772+2332096	0.02 ± 0.02	0.05	0.07	0.08	0.04	-0.02	0.14	0.07	-0.14
2M03481769+2502523	-0.01 ± 0.03	0.01	...	0.09	0.00	0.00	-0.01	-0.10	0.09	0.10	-0.20
2M03403436+2340574	0.09 ± 0.02	0.13	0.10	0.16	0.09	-0.04	0.22	-0.03
2M03474811+2313053	0.03 ± 0.02	0.04	...	0.08	0.03	0.02	0.04	-0.03	0.13	0.15	-0.12
2M03502089+2428003	0.02 ± 0.02	0.03	...	0.02	-0.03	0.02	0.02	-0.05	0.13	0.07	-0.15
2M03454184+2425534	0.05 ± 0.02	0.08	...	0.05	0.07	0.08	0.05	-0.03	0.17	0.20	-0.13
2M03502130+2305470	0.01 ± 0.02	0.04	...	0.14	-0.02	0.02	0.04	-0.08	0.09	0.13	-0.17
2M03444398+2413523	0.00 ± 0.02	0.02	...	0.03	-0.01	0.00	0.03	-0.11	0.07	0.06	-0.18
2M03392780+2353420	0.05 ± 0.03	0.08	-0.12	0.10	0.09	-0.01	0.06	-0.04	0.17	0.18	-0.13
2M03433440+2345429	-0.06 ± 0.02	-0.03	...	0.06	-0.06	-0.03	-0.05	-0.07	0.11	0.03	-0.26
2M03435070+2414508	-0.08 ± 0.02	-0.04	...	0.07	-0.03	0.02	-0.02	-0.07	0.06	0.09	-0.25
2M03470141+2329419	0.03 ± 0.02	0.05	...	0.07	0.01	0.06	0.06	-0.10	0.10	0.10	-0.16
2M03492873+2342440	0.01 ± 0.02	0.02	-0.08	0.06	0.04	0.01	0.03	-0.10	0.11	0.03	...	0.12	-0.20
2M03495035+2342202	0.04 ± 0.02	0.06	-0.14	0.09	0.02	0.04	0.03	-0.09	0.14	0.16	-0.13
2M03505508+2411508	-0.01 ± 0.02	0.01	...	0.08	-0.01	0.02	0.02	-0.10	0.07	0.13	-0.17
2M03532369+2403542	-0.05 ± 0.02	-0.01	...	0.03	0.00	0.00	0.01	-0.09	0.08	-0.03	-0.27
2M03490232+2315088	0.00 ± 0.02	0.01	-0.08	0.03	-0.02	-0.05	0.01	-0.09	0.05	-0.07	-0.21
2M03461174+2437203	-0.06 ± 0.02	-0.06	0.00	0.02	-0.10	-0.03	-0.03	-0.18	0.06	0.00	-0.41
2M03444317+2552319	0.00 ± 0.02	0.02	...	0.03	0.02	0.01	0.00	-0.15	0.10	0.06	...	0.06	-0.22
2M03440484+2416318	-0.01 ± 0.02	0.00	...	0.10	0.03	0.03	-0.02	-0.06	0.09	-0.27
2M03573331+2403114	0.00 ± 0.02	0.00	0.02	0.04	0.02	-0.03	0.01	-0.17	0.05	0.06	...	0.02	-0.20
2M03430293+2440110	0.04 ± 0.02	0.03	-0.04	0.04	0.06	0.02	0.06	-0.08	0.10	0.08	-0.18
2M03450326+2350219	0.02 ± 0.02	0.03	...	0.02	-0.04	-0.04	0.04	-0.09	0.10	0.07	-0.17
2M03513903+2245010	0.00 ± 0.02	0.00	0.05	0.04	0.02	0.02	0.05	-0.14	0.05	0.07	...	0.12	-0.21
2M03363030+2400440	0.02 ± 0.02	0.03	...	0.12	0.02	0.00	0.04	-0.17	0.12	0.01	...	0.08	-0.23
2M03403072+2429143	-0.10 ± 0.02	-0.08	...	0.02	-0.16	...	-0.01	-0.20	0.02	-0.36
2M03444394+2529574	-0.02 ± 0.03	-0.01	-0.12	0.02	-0.08	-0.03	0.02	-0.14	0.10	-0.07	-0.27
2M03470678+2342546	0.05 ± 0.02	0.03	...	0.04	0.12	-0.04	0.01	-0.11	0.06	0.04	...	0.07	-0.21
2M03471480+2522186	-0.06 ± 0.02	-0.06	0.01	0.12	-0.06	...	-0.01	-0.20	0.01	-0.38
2M03434901+2543466	0.00 ± 0.02	-0.01	...	0.03	-0.01	-0.04	-0.03	-0.20	0.07	0.06	0.08	0.01	-0.28
2M03511685+2349357	0.05 ± 0.02	0.06	-0.07	...	0.11	-0.02	0.07	-0.14	0.08	0.06	-0.19
2M03441120+2322455	0.08 ± 0.02	0.00	...	0.06	-0.12	0.00	0.04	-0.18	0.10	-0.11	-0.34
2M03505143+2319447	0.05 ± 0.02	0.05	...	0.05	0.04	0.00	0.07	-0.12	0.10	-0.02	...	0.16	-0.14
2M03452219+2328182	0.04 ± 0.02	0.04	0.03	-0.02	0.04	-0.09	0.02	-0.05	-0.20
2M03440509+2529017	0.01 ± 0.03	-0.02	-0.13	0.01	0.00	-0.07	0.00	-0.17	0.04	...	0.12	0.02	-0.23
2M03404256+2542197	0.00 ± 0.03	-0.02	-0.09	0.06	-0.03	-0.06	-0.01	-0.19	0.03	-0.05	...	0.02	-0.27
2M03471352+2342515	0.04 ± 0.02	0.03	...	0.05	0.04	-0.02	0.00	-0.16	0.09	0.00	0.12	0.05	-0.12
2M03463938+2401468	0.04 ± 0.03	0.06	-0.03	0.09	0.02	-0.06	0.02	-0.03	0.09	0.03	0.01	0.11	...
2M03420470+2553091	0.07 ± 0.02	0.05	...	0.03	0.05	0.01	0.01	-0.12	0.11	-0.04	-0.10	0.13	-0.16
2M03555603+2334021	0.04 ± 0.02	0.05	-0.07	...	0.09	-0.08	0.04	-0.19	0.11	0.01	0.12	0.07	-0.17
2M03415906+2555153	0.05 ± 0.02	0.04	0.08	-0.06	0.05	-0.17	0.10	0.00	-0.10	0.10	-0.17
2M03422759+2502492	0.05 ± 0.03	0.05	...	0.06	0.06	0.00	0.05	-0.10	0.12	-0.03	...	0.04	-0.15
2M03460649+2434027	0.06 ± 0.03	0.05	-0.05	0.05	0.02	-0.02	0.05	-0.19	0.10	0.05	0.08	0.10	-0.16
2M03503457+2430281	0.02 ± 0.03	0.02	...	0.07	0.01	-0.04	0.03	-0.12	0.04	-0.03	...	-0.02	-0.19
2M03401202+2538321	-0.10 ± 0.03	-0.08	0.02	0.10	-0.09	...	-0.03	0.08
2M03513927+2432561	0.03 ± 0.03	0.02	...	0.04	0.01	-0.08	0.06	-0.19	0.01	-0.07	...	0.09	-0.23
2M03540892+2420011	-0.01 ± 0.03	0.00	-0.04	0.07	-0.02	...	0.03	-0.23	0.02	-0.16	...	-0.04	-0.20
2M03413245+2309422	0.02 ± 0.01	0.02	...	0.06	0.00	-0.07	-0.02	-0.16	0.03	-0.09	...	-0.10	...
2M03452957+2345379	0.05 ± 0.03	0.05	...	0.03	0.07	-0.11	0.05	-0.15	0.09	-0.02	...	0.16	-0.13
2M03405126+2335543	0.08 ± 0.03	0.08	0.13	-0.01	0.02	-0.15	0.08	0.00	0.10	0.13	-0.16
2M03432662+2459395	0.01 ± 0.04	0.03	...	0.08	0.02	-0.05	0.02	-0.09	0.06	-0.08	-0.10	0.05	...
2M03455048+2352262	0.03 ± 0.03	0.04	-0.16	...	-0.04	-0.02	0.03	-0.23	0.04	-0.04	-0.04	0.09	-0.19
Mean Cluster values	0.03	0.03	-0.06	0.07	-0.01	0.00	0.03	-0.09	0.10	-0.01	0.03	0.08	-0.18
Median Cluster values	0.03	0.04	-0.07	0.06	0.00	0.00	0.03	-0.09	0.10	0.00	0.08	0.09	-0.18
Median Absolute Deviation (MAD)	0.02	0.02	0.08	0.04	0.04	0.02	0.02	0.06	0.03	0.00	0.08	0.07	0.05
Standard deviation of the mean	0.05	0.04	0.06	0.04	0.07	0.07	0.03	0.08	0.05	0.06	0.09	0.08	0.08
Propagated Uncertainties (mean values)	0.06	0.06	0.03	0.07	0.10	0.08	0.07	0.03	0.05	0.06	0.06	0.05	0.04

4 RESULTS

In this section, we present abundance results for twelve elements (C, Na, Mg, Al, Si, K, Ca, Ti, V, Cr, Mn, and Fe) in 80 F, G, and K dwarf stars from the Pleiades open cluster. The individual stellar abundances are presented in Table 3, where the mean abundances, standard deviations, and uncertainties obtained for the cluster are presented in the last lines of Table 3.

We derived metallicities using two methods: BACCHUS in semi-automatic mode and an MCMC analysis. Through our abundance analysis using BACCHUS, we derived a mean iron abundance (a proxy for metallicity) for the cluster of $\langle [\text{Fe}/\text{H}] \rangle = 0.03 \pm 0.04$ dex, indicating that the Pleiades open cluster is slightly metal-rich. Using a two-dimensional MCMC analysis that considers both $[\text{Fe}/\text{H}]$ and $v\sin(i)$, we obtained the same mean metallicity result with a slightly higher standard deviation: $\langle [\text{Fe}/\text{H}] \rangle = 0.03 \pm 0.05$ dex. In Figure 2, the upper panel provides a direct comparison of our BACCHUS derived $[\text{Fe}/\text{H}]$ (x-axis) with that obtained from MCMC (y-axis). The color bar denotes T_{eff} , while the lower panel illustrates the residual difference between $[\text{Fe}/\text{H}]$ from semi-automatic BACCHUS analysis and $[\text{Fe}/\text{H}]$ from MCMC. Our results demonstrate excellent agreement in the metallicity scale, with $[\text{Fe}/\text{H}](\text{BACCHUS} - \text{MCMC}) = 0.01 \pm 0.02$ dex, and we see no systematic trends with T_{eff} . In conclusion, the derived metallicities are consistent across methods, and these results align well with previous measurements from the literature (Soderblom et al. 2009; Takeda, Hashimoto & Honda 2016; Spina et al. 2018).

For the overall metal content of the cluster, denoted as $[\text{M}/\text{H}]$, we calculate a value of 0.01 ± 0.06 , reinforcing iron as a reliable proxy for the cluster metallicity. The average alpha-element to iron abundance ratio, calculated as the mean of $[\text{Mg}/\text{Fe}]$, $[\text{Si}/\text{Fe}]$, and $[\text{Ca}/\text{Fe}]$, is $[\alpha/\text{Fe}] = 0.01 \pm 0.05$. For odd- z elements (Na, Al, K), we find $[\text{odd-}z/\text{Fe}] = -0.04 \pm 0.08$, and for the iron-peak elements V, Cr, and Mn, $[\text{iron peak}/\text{Fe}] = -0.02 \pm 0.08$. These values, indicative of yields from both Type I and II supernovae, approach solar levels—an unsurprising result, given the Pleiades' proximity to the Sun (135 pc; Lodieu et al. 2019) and its relative youth (112 Myr; Dahm 2015). We reference solar abundance values from Asplund et al. (2021).

Examining the individual elements, we find their abundances to be in close proximity to solar values, such as $[\text{Ti}/\text{H}] = -0.01 \pm 0.06$, $[\text{Mg}/\text{H}] = 0.00 \pm 0.07$, $[\text{Al}/\text{H}] = 0.00 \pm 0.07$, $[\text{Si}/\text{H}] = 0.03 \pm 0.03$, and $[\text{V}/\text{H}] = 0.03 \pm 0.09$. Some elements exhibit slightly enhanced abundances, including $[\text{Na}/\text{H}] = 0.07 \pm 0.04$, $[\text{Cr}/\text{H}] = 0.08 \pm 0.08$, and $[\text{Ca}/\text{H}] = 0.10 \pm 0.05$ dex. Others show slightly depleted abundance ratios, such as $[\text{C}/\text{H}] = -0.06 \pm 0.06$, $[\text{Mn}/\text{H}] = -0.08 \pm 0.08$ dex, and $[\text{K}/\text{H}] = -0.09 \pm 0.08$. Table 3 lists the stellar abundances determined in this study.

4.1 Comparisons with the literature

4.1.1 APOGEE DR17

In this section, we compare our results with those from SDSS-IV APOGEE DR17. While APOGEE primarily targeted red giants, it also included numerous main-sequence stars. Although the SDSS-IV has ended, DR17 results are used by the community, and the ASPCAP pipeline continues to be used as one of the pipelines for parameters and abundance determinations in the ongoing SDSS-V Milky Way Mapper (MWM) survey, that now has an important component focusing on main-sequence stars. Consequently, our results can provide valuable calibration data for the abundances derived by their pipelines.

The comparison of our computed $v\sin(i)$ using MCMC (x-axis)

and those from APOGEE DR17 (y-axis) is shown in the lower panel of Figure 2. The results generally agree, with minor scatter, $v\sin(i)$ (this work - APOGEE DR17) = $0.45 \pm 0.94 \text{ km.s}^{-1}$. There is a noticeable trend in $v\sin(i)$ as a function of T_{eff} , where warmer F-dwarfs exhibit higher $v\sin(i)$ ($\gtrsim 20 \text{ km.s}^{-1}$) compared to cooler K-dwarfs, which show lower values ($\lesssim 10 \text{ km.s}^{-1}$).

Figure 3 presents a one-to-one abundance diagram, plotting our results on the x-axis versus APOGEE DR17 (uncalibrated), Soderblom et al. (2009), and Spina et al. (2018) results on the y-axis. (This section focuses on the comparisons with DR17, while Section 4.1.2 will compare with results from the optical.) Each subplot's bottom panel shows the residual difference (δ) between our work and APOGEE DR17, with a color bar indicating T_{eff} . The comparison of the abundance results generally shows good agreement, particularly for Ca (δ (this work - literature) = 0.04 ± 0.02), Cr ($\delta = -0.02 \pm 0.06$), Mn ($\delta = 0.01 \pm 0.05$), and Fe ($\delta = 0.05 \pm 0.03$). However, some elements like C ($\delta = 0.00 \pm 0.10$), K ($\delta = 0.04 \pm 0.08$) and Mg ($\delta = 0.13 \pm 0.08$) exhibit more scatter, and Na ($\delta = 0.28 \pm 0.16$) shows significant difference. However, it is clear from the figure that the DR17 results for C, Na, Mg, Si, and K show a systematic decrease in the abundances, which is more pronounced for stars with lower T_{eff} , as seen from the light-colored circles, while this work results (x-axis) are clumped around 0.00. This suggests that DR17 may exhibit abundance trends influenced by effective temperature, as discussed in Section 5.1.

It is notable that the Na abundances for the studied Pleiades stars in DR17 have very large offsets and systematic trends; Na abundances are derived from two weak lines in the APOGEE spectra. These systematic trends may be attributed to the challenges ASPCAP faces in accurately measuring weak lines. Such trends result in mean Na abundances with very large scatter, which is not expected for stars in an open cluster (standard deviation of the mean of 0.23). In contrast, in this work, we obtain a much more reasonable standard deviation of the mean $A(\text{Na})$ of 0.04 for the studied Pleiades stars.

4.1.2 Optical high-resolution abundance studies

The Pleiades is one of the most studied open clusters in our Galaxy. Despite this, there remains a lack of comprehensive abundance studies spanning the cluster's extensive range of stellar masses. Previous studies have primarily focused on the cluster's luminous peculiar stars. Notably, Hui-Bon-Hoa & Alecian (1998) and Gebran & Monier (2008) have conducted abundance analyses on A-type stars, both normal and chemically peculiar (Am), as well as F-type stars using high-resolution optical spectroscopy. These studies determined abundances for a variety of elements, including C, N, O, Na, Mg, Si, Ca, Sc, Ti, V, Cr, Mn, Fe, Co, Ni, Sr, Y, Zr, and Ba. Additionally, Soderblom et al. (2009) and Takeda, Hashimoto & Honda (2016) have characterized the abundances of C, O, Na, Fe, Si, Ni, and Ti in FGK dwarf stars, also employing high-resolution optical spectra.

More recently, Spina et al. (2018) explored chemical inhomogeneities in the Pleiades, potentially caused by planetary engulfment. The authors utilized high-resolution spectroscopy from the UVES at the Very Large Telescope of the European Southern Observatory. The five stars studied by Spina et al. (2018) are also examined in this work: 2M03385686+2434112, 2M03440424+2459233, 2M03450400+2515282, 2M03465491+2447468, and 2M03491172+2438117. This work's atmospheric parameters show good agreement with Spina et al. (2018), where $\delta T_{\text{eff}} = -31 \pm 39\text{K}$, and $\delta \log g = -0.06 \pm 0.04$ dex (δ represents the mean difference, This Work - Spina et al. 2018). Overall, our abundance results agree well with their results, as shown by the yellow diamond symbols in Figure 3. Elements exhibiting significant disparities in

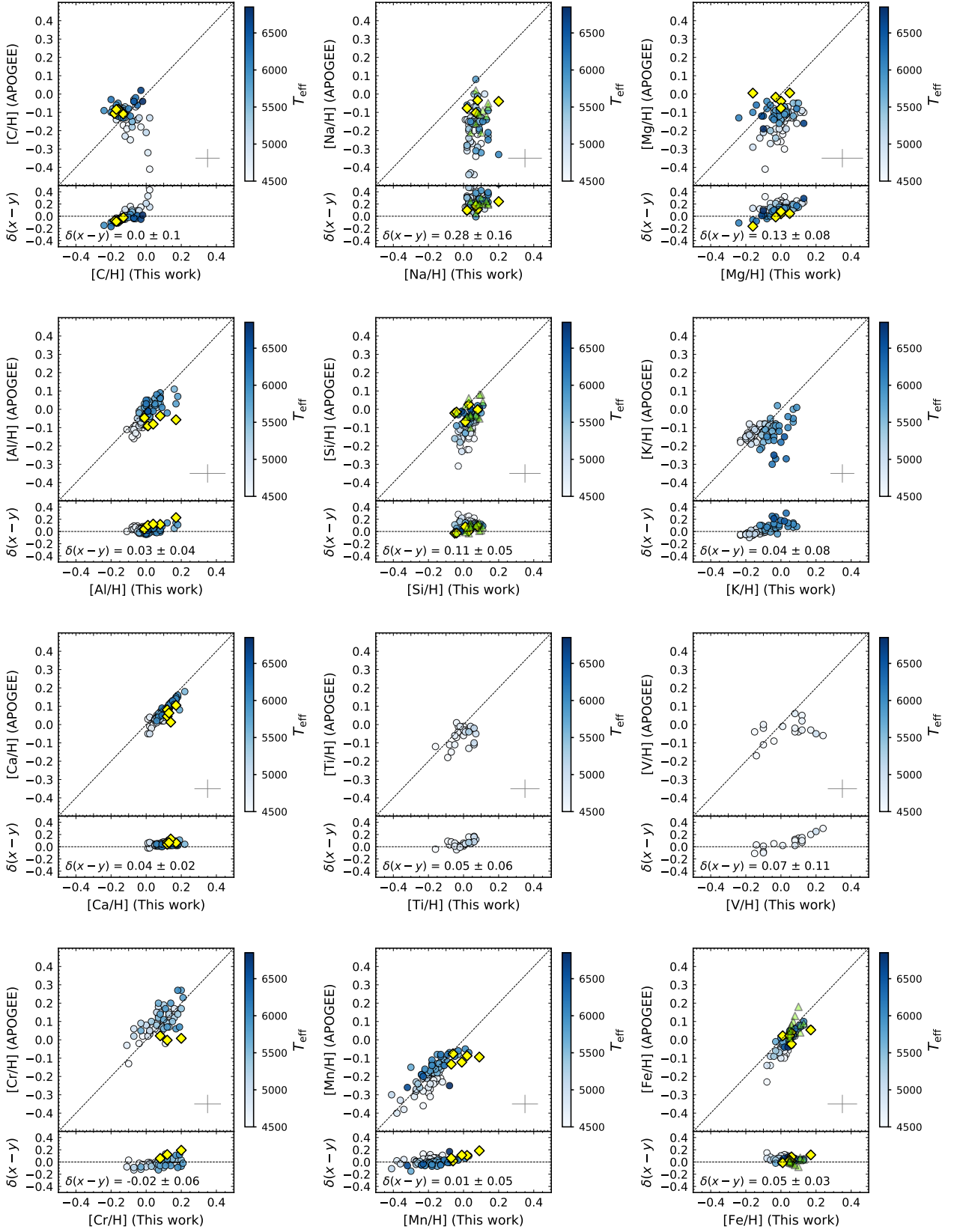


Figure 3. Abundance comparisons of this work and those from the literature (APOGEE DR17, circles with color bar; Spina *et al.* (2018) as a yellow diamond; Soderblom *et al.* (2009) as a green triangle). Each panel represents an individual element. Same format as Figure 2.

this comparison are Na ($\delta = 0.16 \pm 0.06$), Al ($\delta = 0.12 \pm 0.06$), Cr ($\delta = 0.12 \pm 0.05$), and Mn ($\delta = 0.10 \pm 0.06$). The presence of weak lines in the APOGEE spectra for Na and Cr within the atmospheric parameter range of our studied sample may indicate additional challenges in measuring their abundances. Elements like C, Mg, Si, and Fe exhibit mean abundance differences smaller than 0.06 dex, indicating a good agreement within the uncertainties.

Thirteen F and G dwarfs in this work were previously studied in Soderblom et al. (2009). (They are marked on Table 1). The latter study determined abundances of Fe, Si, Ni, Ti, and Na from the Hamilton optical echelle high-resolution spectrograph ($R=40,000$) in 20 Pleiades solar-like stars having low $v \sin(i)$ values. Comparisons between our results and those from Soderblom et al. (2009) generally show good agreement, with $\delta[\text{Fe}/\text{H}] = 0.00 \pm 0.04$ and $\delta[\text{Si}/\text{H}] = 0.06 \pm 0.06$. However, a notable discrepancy exists for Na, where $\delta[\text{Na}/\text{H}] = 0.21 \pm 0.06$, indicating significantly lower values in Soderblom et al. (2009), as seen in Figure as a green triangle in Figure 3. The observed offset in Na abundances between this study and those reported by Soderblom et al. (2009) and Spina et al. (2018) could be attributed to non-LTE effects impacting the optical Na I lines used in their analyses, as these may be significantly affected by departures from LTE (Asplund 2005).

5 DISCUSSION

5.1 Abundance trends as a function of T_{eff}

In Figure 4 left panels, we illustrate how magnesium abundances change with T_{eff} for two specific Mg I lines: the stronger line $\lambda 15748.988 \text{ \AA}$ (top panel) and the weaker line $\lambda 15879.5 \text{ \AA}$ (bottom panel). For the stronger line, we see that as T_{eff} decreases, the Mg abundance derived from the line $\lambda 15748.988 \text{ \AA}$ declines strongly. For T_{eff} values exceeding 6000K, the Mg abundances do not follow the same trend, becoming approximately constant. In contrast, the bottom-left panel shows the behavior of the Mg abundances derived from the weaker Mg I line at $\lambda 15879.5 \text{ \AA}$. Here we see no significant trend of the Mg abundances as a function of T_{eff} .

On the right panel of Figure 4, we display the synthetic line profiles of these Mg I lines for T_{eff} s ranging from 4500 to 7000 K in steps of 250 K, while fixed values for $\log g = 4.50$, $\xi = 1.0 \text{ km.s}^{-1}$, and $[\text{Fe}/\text{H}] = 0.00$ are adopted. The yellow-ish solid lines indicate warmer, and the purple-ish solid lines represent cooler stars with their respective spectral synthesis. For the top-right panel, we see the Mg I line profiles getting broader at the wings and having a significant pseudo-continuum suppression of each line as T_{eff} decreases. As a consequence, the FWHM for K dwarfs is about twice that of those late F dwarfs. The observed line broadening profile is primarily influenced by the rise in atomic collisions in the stellar atmosphere as stars become more compact along the cooler main sequence. In the bottom-right panel, we can see that the line broadening and pseudo-continuum depletion for the weaker Mg I at $\lambda 15879.5 \text{ \AA}$ are considerably smaller compared to the top-right panel.

We find a similar trend for the Mg abundances derived from the Mg I lines at $\lambda 15740.716 \text{ \AA}$, and $\lambda 15765.84 \text{ \AA}$ similarly to Figure 4 top left panel. However, the Mg I lines at $\lambda 15886.2 \text{ \AA}$ and $\lambda 15954.477 \text{ \AA}$ do not exhibit a substantial trend with T_{eff} and resemble the behavior seen in the bottom-left panel of Figure 4. Given that the Mg abundance of stars in an open cluster are not expected to vary, it appears that a physical or analytical factor strongly influences the profiles of the Mg I lines at $\lambda 15740.176 \text{ \AA}$, $\lambda 15748.988 \text{ \AA}$, and $\lambda 15765.842 \text{ \AA}$, and we are compensating this effect by changing the Mg abundances

to roughly fit the lines. In Appendix A1, we list all spectral lines adopted in this study that exhibit no or weak abundance trends with T_{eff} , as well as those lines excluded due to strong trends with T_{eff} .

A comparison of the relative line strengths between the included and excluded lines in Appendix A1, within each element, reveals that the excluded lines are the stronger lines (the division is quite striking for C I, Mg I, Al I, Si I, and Ti I). As the stronger lines will form higher in the stellar atmospheres, the trends with T_{eff} may be related to the depth-of-formation and perhaps involve non-LTE (although in our case, departures from LTE are small) or, for example, be related to inadequacies in our treatment of line broadening.

As discussed above, in this study, we only use selected lines with small or no significant abundance trends with the effective temperature (see Appendix A1). Figure 5 provides a visual overview of all of the elemental abundances determined here as a function of effective temperature. Beginning with Fe, whose abundance is derived from the largest number of lines (31), no trend is found within a small abundance scatter of $\sim \pm 0.05$ dex. Carbon abundances rely on two rather weak C I lines that are measured here over a somewhat restricted T_{eff} range and display no measurable trend with temperature. The odd-Z elements Na and Al are represented by only 2 lines and 1 line, respectively, with the Na I lines being quite weak, while the Al I line is stronger and well-defined. Both sets of abundances exhibit insignificant slopes (within our measurement uncertainties). We can see that the selected Mg I lines in this study (as discussed above) resulted in Mg abundances without significant trends with temperature, while the cluster Si abundances, in particular, are characterized by a small scatter of ± 0.03 dex. Titanium and vanadium are both measured over a narrow range in effective temperature such that any inherent dependencies on T_{eff} are not detected. The remaining four elements, K, Ca, Cr, and Mn, all display only small T_{eff} trends that result in increasing abundances with increasing temperature and all having slopes of $\sim +0.1$ dex or less per 1000 K. Chromium abundances based upon the APOGEE spectra can be, in general, uncertain due to the fact that Cr abundances are based on one weak Cr I line, which can be impacted by any nearby weak unidentified features. The other elemental abundances that decrease slightly with decreasing temperature (K, Ca, and Mn) are derived from well-defined lines with weak to moderate line strengths. These results highlight the usefulness of open clusters as checks on the spectroscopic analyses of dwarf stars using the APOGEE spectra.

5.2 Investigating potential causes of abundance trends

Line profile fitting

To investigate possible systematic errors in the best-fit syntheses in our abundance measurements across different stellar classes, we compared the fits obtained for a warmer F- and a cooler K-dwarf. This is illustrated in Figure 6, which displays our synthetic best fits for the Mg I line at $\lambda 15748.988 \text{ \AA}$ in two stars with different effective temperatures: 2M03385686+2434112 ($T_{\text{eff}} = 6029 \text{ K}$) and 2M03455048+2352262 ($T_{\text{eff}} = 4502 \text{ K}$). The APOGEE spectra of both stars have very high SNR, 530 and 217, respectively. The crosses and dashed black line represent the observed and best-fit spectra for 2M03385686+2434112, respectively, while the open circles and solid black line represent the observed and best-fit spectra for 2M03455048+2352262. Our syntheses reproduce the Mg I lines with fidelity. For example, the chi-square obtained for 2M03385686+2434112 is 14.0, and for 2M03455048+2352262, it is 5.8, which is quite similar, even though the line intensity changes for both stars. As illustrated in the right panels of Figure 4, we also see

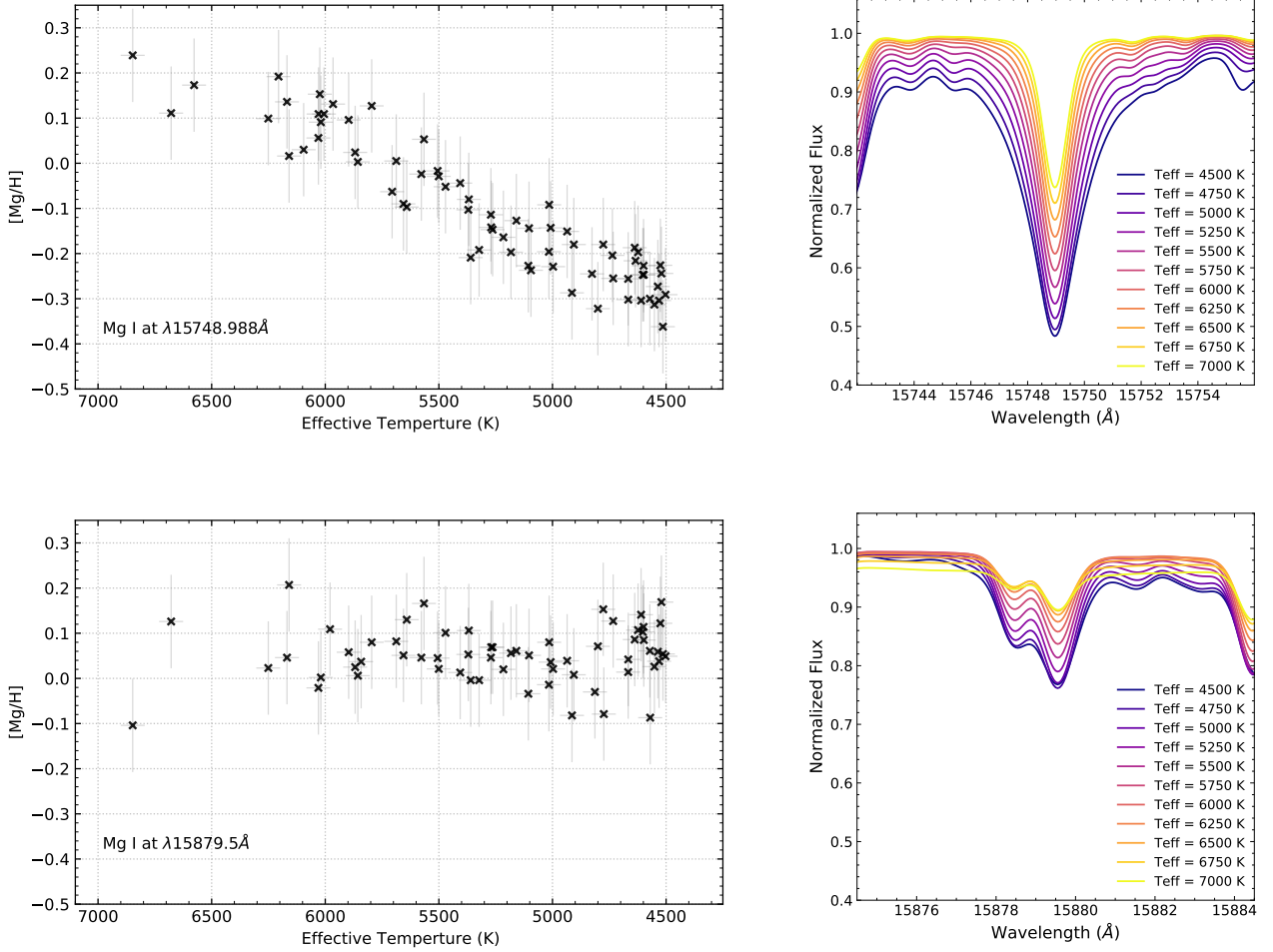


Figure 4. Left panel: Values of $[\text{Mg}/\text{H}]$ vs. T_{eff} , with the left upper panel showing abundances derived from the Mg I line at $\lambda 15748.988 \text{ \AA}$, while the left lower panel shows results for the $\lambda 15879.5 \text{ \AA}$ line. Right panel: Spectral syntheses for different values of T_{eff} , ranging from 4500 to 7000 K in steps of 250 K, assuming fixed values for $\log g = 4.50$, $\xi = 1.0 \text{ km.s}^{-1}$, and $[\text{Fe}/\text{H}] = 0.00$. The right upper panel shows the Mg I line at $\lambda 15748.988 \text{ \AA}$, and the right lower panel shows the Mg I line at $\lambda 15879.5 \text{ \AA}$.

that the wings of the cooler main sequence stars are broader, where the equivalent width (EW) is 1550.8 m\AA for 2M03455048+2352262, in contrast with 803.2 m\AA for 2M03385686+2434112. The lower T_{eff} star 2M03455048+2352262 presents a slightly lower pseudo-continuum of the line $\lambda 15748.988 \text{ \AA}$ compared to the warmer star 2M03385686+2434112.

Departures from LTE and use of a different radiative transfer code

The observed abundance trend for certain spectral lines may result from several factors, one of which is deviations from the local thermodynamical equilibrium. As discussed in Section 3.6, the majority of lines analyzed in this study showed negligible deviations from LTE (~ 0.01 dex for most), and these cannot explain the spurious abundance trends observed for certain lines. Manganese lines exhibited more significant departures from LTE (around 0.10 dex), however, such deviations remained roughly constant across the T_{eff} range of our Pleiades sample. Finally, some abundance trends might be attributed to the need for a more comprehensive abundance analysis, combining non-LTE and 3D effects. However, these corrections are

expected to be minimal for G and K-dwarfs (Osorio et al. 2020; Asplund et al. 2021, and references therein).

To investigate if a different radiative transfer code and model atmosphere grid would predict different profiles for the Mg I lines, we derived Mg abundances for ten representative stars covering a range in effective temperature (2M03455048+2352262, 2M03513903+2245010, 2M03450326+2350219, 2M03454184+2425534, 2M03502089+2428003, 2M03483451+2326053, 2M03462735+2508080, 2M03462777+2335337, 2M03491230+2313421, 2M03462862+2445323) using the 1D LTE radiative transfer code MOOG (Snedden et al. 2012) with Kurucz atmospheric models (Castelli & Kurucz 2003) and Turbospectrum with Kurucz atmospheric models. The MOOG/Kurucz derived Mg abundances remained similar to the ones from this study, which were derived with Turbospectrum/MARCS, and, in particular, the strong Mg I lines displayed similar trends of $A(\text{Mg})$ versus T_{eff} as before, with the K dwarfs having significantly lower abundances than F and G dwarfs.

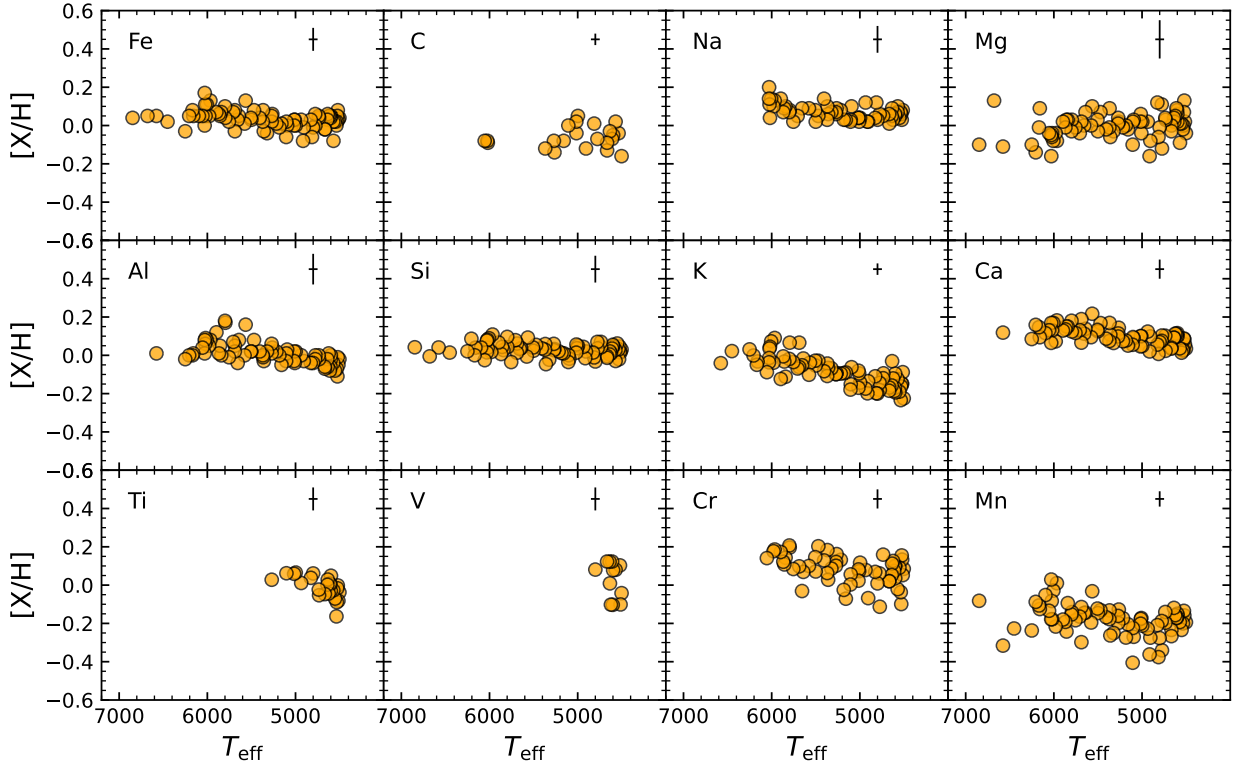


Figure 5. Derived abundances ($[X/H]$) of the studied stars as a function of effective temperature.

Systematic uncertainties in the adopted parameters

Systematic errors in stellar parameters often cause trends in abundance results. We used the sensitivity table for abundance changes due to uncertainties in the T_{eff} and $\log g$ to assess the parameter changes needed to align the Mg abundances from the Mg I lines $\lambda 15740.716$ Å, $\lambda 15748.988$ Å, and $\lambda 15765.842$ Å of K dwarfs with those of F dwarfs. Our analysis indicated that achieving similar Mg abundances would require reducing T_{eff} by ~ 900 K and $\log g$ by ~ 0.6 dex. Such systematic changes are completely out of the uncertainties in the stellar parameters, and we conclude that this is not a viable solution to the abundance trend problem.

Extra broadening due to Zeeman splitting

Young stars, such as those members of the Pleiades open cluster, are known to be more active and have magnetic fields. The influence of stellar activity or magnetic fields in these stars could introduce extra broadening in those line profiles corresponding to transitions that are sensitive to magnetic fields (see Barrado y Navascués et al. 2001; Wanderley et al. 2024). In this regard, we compiled Landé g -factors for all lines analyzed in this work to investigate potential correlations between the observed abundance and Landé factors. Our analysis found no correlation between the Landé g values and the observed abundance trends, suggesting that the abundance trends are not related to the effects of the stellar magnetic fields.

Changing the broadening parameters in the line list

Under the reasonable assumption that the chemical abundances in open clusters are homogeneous, we adopt the Mg abundance obtained

for a solar-type star from our sample as representative of the Mg abundance for the Pleiades cluster. This choice is made because the Sun was used as the benchmark star to fine-tune damping constants for strong lines in the APOGEE line list, as discussed in Smith et al. (2021).

We analyzed the spectrum of a K-dwarf ($T_{\text{eff}} \sim 4500$ K) from our sample, and, adopting the reference Mg abundance from the solar-type star, we adjusted the van der Waals damping values for the three strong Mg I lines at $\lambda 15740.716$ Å, $\lambda 15748.988$ Å, and $\lambda 15765.842$ from their default values in the line list by -0.52 , -0.47 , and -0.68 , respectively. These adjustments in the damping led to sharper line profiles, and we note that in order to achieve good fits between observed and synthetic spectra, small additional adjustments in the adopted Gaussian broadening representing the APOGEE spectrograph LSF were required. We did the same test for an F-dwarf ($T_{\text{eff}} \approx 6500$ K) from our sample, and this resulted in small positive changes of $+0.14$, 0.20 , and 0.13 in the damping values of the Mg I lines at $\lambda 15740.716$ Å, $\lambda 15748.988$ Å, and $\lambda 15765.842$ Å, respectively. As previously discussed, it is clear that the stronger the spectral line, the larger the discrepancy in the modeled line profiles in comparison with the observations if the elemental abundance is kept constant, and consequently, when allowing the abundance to vary, the more pronounced is the trend with T_{eff} .

5.3 Limits on atomic diffusion in the Pleiades stars

Atomic diffusion is a significant physical process, theoretically described (Michaud, Alecian & Richer 2015), occurring in all stars but more dominant in certain evolutionary stages. Generally, atomic diffusion competes with other hydrodynamic transport processes that can neutralize its effect, with convection being the most significant.

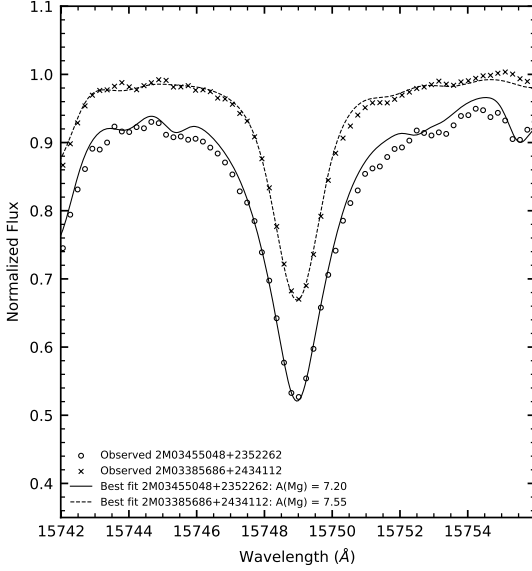


Figure 6. A small portion of two APOGEE spectra displaying a single spectral line with the observed and best-fit synthetic spectra for an F-dwarf (2M03385686+2434112; crosses show the observed spectrum and the dashed black line the best-fit spectrum) and a K-dwarf (2M03455048+2352262; circles represent the observed data and the solid black line is the best-fit synthetic spectrum), centered on the Mg I line at $\lambda 15748.988\text{\AA}$.

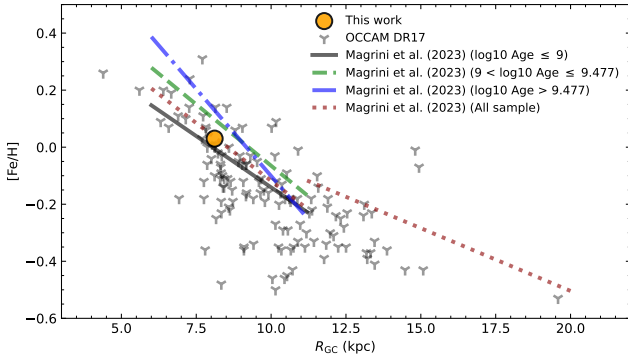


Figure 7. Stellar metallicity as a function of galactocentric distance (kpc). Our metallicity result for the Pleiades (filled orange circle) plotted along with the OCCAM results, shown as grey symbols, with the different lines representing abundance gradient slopes for different ages from Magrini et al. (2023).

Typically, the timescale of convection is orders of magnitude shorter than that of diffusion, thereby significantly diminishing the diffusion effect in convective regions. The condition for efficient diffusion is the absence of other significant transport processes, such as convection, turbulent motions, radiative winds, accretion, and mass loss. For instance, diffusion is expected to operate efficiently in the radiative zones of solar-type or warmer main-sequence stars, where gravitational settling is effective due to reduced convective motion. However, when solar-type stars evolve into the red giant stage, the effects of diffusion become much less significant (Michaud, Alecian & Richer 2015), primarily because the convective zone significantly expands.

It is expected that the young Pleiades open cluster members do not exhibit large atomic diffusion effects (Dotter et al. 2017). The

MIST isochrone model, which incorporates atomic diffusion for solar metallicity at the age of 112 Myr (Choi et al. 2016), predicts an iron abundance depletion of approximately $[\text{Fe}/\text{H}] = 0.02$ dex at T_{eff} around 6500K. Although such a small abundance depletion would not be measurable in this study, given our internal iron abundance uncertainties of $\sim 0.05 - 0.06$ dex, the few warmer F stars in our sample ($T_{\text{eff}} \sim 6500\text{K}$) do not show any statistically significant evidence of depletion beyond the estimated uncertainties (see Figure 5). The absence of detectable diffusion beyond ~ 0.05 dex is overall in line with the model predictions.

5.4 The results for the Pleiades in the context of Galactic metallicity gradients

Open clusters are important probes in defining the metallicity gradients of the Galactic thin disk (e.g., Frinchaboy et al. 2013; Cunha et al. 2016; Casamiquela et al. 2021; Spina, Magrini, & Cunha 2022). In Figure 7, we present the galactocentric distance (in kpc) versus metallicity for various galactic open clusters (grey symbols), based on data from the OCCAM survey (Myers et al. 2022); the mean metallicity obtained in this study for the Pleiades stars is shown as the filled orange circle. To compare the position of the Pleiades open cluster with metallicity gradients from the literature, we show the results from Magrini et al. (2023), which come from the open cluster sample in the Gaia-ESO survey. Different gradients in that study were obtained for open clusters in different age bins: the black line represents clusters younger than 1 Gyr, the green-dashed line open clusters having ages between 1 and 3 Gyr, and the dot-dashed blue line represents ages higher than 3 Gyr. The dotted brown line illustrates the gradient for all the open cluster samples from Magrini et al. (2023) ($[\text{Fe}/\text{H}] = -0.081 \times R_{\text{GC}} + 0.692$ for $R_{\text{GC}} \leq 11.2$ kpc and $[\text{Fe}/\text{H}] = -0.044 \times R_{\text{GC}} + 0.376$ for $R_{\text{GC}} > 11.2$ kpc). Notably, our result for the Pleiades is in line with the overall position of the OCCAM open clusters in a similar galactocentric distance. It intersects the overall regression line (brown dashed line), falling slightly above the line representing the gradients for clusters younger than 1 Gyr (black line).

6 CONCLUSIONS

Open clusters serve as essential astrophysical laboratories for examining physical processes during stellar evolution. They provide unique opportunities to validate methodologies for determining stellar abundances across stars with varied masses, effective temperatures, and surface gravities. Analyzing how stellar abundances correlate with stellar parameters and evolutionary stages can reveal systematic errors in abundance determinations or reveal signatures of abundance variations.

This paper presents a comprehensive study of the abundances of C, Na, Mg, Al, Si, K, Ca, Ti, V, Cr, Mn, and Fe in 80 F, G, and K main-sequence dwarf members of the Pleiades open cluster, utilizing high-resolution APOGEE spectra. Our sample spans an effective temperature range of ~ 4500 to 6850 K. Despite being one of the most extensively studied open clusters, the Pleiades previously lacked a detailed abundance analysis of many elements covering a wide range of stellar masses as presented here.

The mean metallicity obtained for the studied Pleiades sample is roughly solar, $[\text{Fe}/\text{H}] = 0.03 \pm 0.04$ dex. The mean element-over-iron abundance ratios derived for the different nucleosynthetic families are as follows: $[\alpha/\text{Fe}] = 0.01 \pm 0.05$, $[\text{odd-}z/\text{Fe}] = -0.04 \pm 0.08$, and $[\text{iron peak}/\text{Fe}] = -0.02 \pm 0.08$. All these abundance ratios agree with

expectations for the chemistry of a roughly solar metallicity open cluster from the solar neighborhood. In addition, the mean metallicity obtained for the Pleiades are in line with metallicity gradients from open clusters in the literature.

The detailed line-by-line modeling presented for the studied Pleiades dwarfs, which cover a wide range in effective temperature of more than 2000 K, was an effective tool in revealing inadequacies in the modeling of strong lines in the APOGEE region when using the current abundance analysis codes and the APOGEE line list. Allowing the elemental abundances to vary in order to compensate for mismatches between synthesis and observations resulted in derived abundances having strong trends with the effective temperature, for example, for the three strong Mg I lines at $\lambda 15740.716\text{\AA}$, $\lambda 15748.988\text{\AA}$, and $\lambda 15765.842\text{\AA}$.

One important result of this paper is the compilation of selected spectral lines (Table A1), which are deemed to be good abundance indicators and to provide abundances that are nearly independent of the effective temperature for F, G, and K dwarfs. The APOGEE abundance pipeline ASPCAP derives abundances by fitting, at the same time, all selected lines available for a specific element, and as thus, is also affected by the inadequate modeling of strong lines in the APOGEE spectra, in particular for K dwarfs.

We performed several tests on the strong Mg I lines to probe the observed abundance trends with the effective temperature, such as using different radiative transfer codes or stellar atmosphere models, evaluating if realistic changes in the stellar parameters would erase the abundance trends, investigating non-LTE effects for all studied lines, examining possible trends of abundances with Landé g factors, and adjusting the van der Waals damping constants while keeping the Mg abundance constant. Only the latter could reproduce the observed line profiles, suggesting inadequacies in the spectral line broadening, especially for the cooler K dwarfs, as a possible cause of the spurious trends. However, further work involving K dwarf members from other open clusters is needed in order to explore this possibility carefully.

ACKNOWLEDGEMENTS

We thank the referee for suggestions that improved the paper significantly. D.S. and R.V. thank the National Council for Scientific and Technological Development – CNPq process No. 404056/2021-0. K.C. acknowledges support from the National Science Foundation through NSF grant No. AST-2206543. F.W. acknowledges support from fellowship by Coordenação de Ensino Superior - CAPES. RG gratefully acknowledges the grants support provided by ANID Fondecyt Postdoc No. 3230001 and FAPERJ under the PDR-10 grant number E26-205.964/2022. SD acknowledges CNPq/MCTI for grant 306859/2022-0.

Funding for the Sloan Digital Sky Survey IV has been provided by the Alfred P. Sloan Foundation, the U.S. Department of Energy Office of Science, and the Participating Institutions. SDSS-IV acknowledges support and resources from the Center for High-Performance Computing at the University of Utah. The SDSS website is www.sdss.org. SDSS-IV is managed by the Astrophysical Research consortium for the Participating Institutions of the SDSS Collaboration including the Brazilian Participation Group, the Carnegie Institution for Science, Carnegie Mellon University, the Chilean Participation Group, the French Participation Group, Harvard-Smithsonian Center for Astrophysics, Instituto de Astrofísica de Canarias, The Johns Hopkins University, Kavli Institute for the Physics and Mathematics of the Universe (IPMU) / University of Tokyo, Lawrence Berkeley National Laboratory, Leibniz Institut für Astrophysik Potsdam (AIP), Max-

Planck-Institut für Astronomie (MPIA Heidelberg), Max-Planck-Institut für Astrophysik (MPA Garching), Max-Planck-Institut für Extraterrestrische Physik (MPE), National Astronomical Observatory of China, New Mexico State University, New York University, University of Notre Dame, Observatório Nacional / MCTI, The Ohio State University, Pennsylvania State University, Shanghai Astronomical Observatory, United Kingdom Participation Group, Universidad Nacional Autónoma de México, University of Arizona, University of Colorado Boulder, University of Oxford, University of Portsmouth, University of Utah, University of Virginia, University of Washington, University of Wisconsin, Vanderbilt University, and Yale University.

Facilities: Sloan.

Software: BACCHUS (Masseron, Merle & Hawkins 2016), Turbospectrum (Alvarez & Plez 1998; Plez et al. 2012; <https://github.com/bertrandplez/Turbospectrum2019>).

DATA AVAILABILITY

We utilize data from the final public data release of the SDSS-IV/APOGEE, specifically DR17. The data are publicly available in https://www.sdss4.org/dr17/irspec/spectro_data/.

REFERENCES

- Abazajian K. et al., 2005, *AJ*, 129, 1755
- Abdurro'uf et al., 2022, *ApJS*, 259, 35
- Abolfathi B. et al., 2018, *ApJS*, 235, 42
- Abramson G., 2018, *RNAAS*, 2, 150
- Adelman-McCarthy J. K. et al., 2006, *ApJS*, 162, 38
- Adelman-McCarthy J. K. et al., 2007, *ApJS*, 172, 634
- Allende Prieto C. et al., 2006, *ApJ*, 636, 804
- Allende Prieto C. et al., 2014, *A&A*, 568, A7
- Alvarez R., Plez B., 1998, *A&A*, 330, 1109
- Asplund M., 2005, *ARA&A*, 43, 481.
doi:10.1146/annurev.astro.42.053102.134001
- Asplund M., Amarsi A. M., Grevesse N., 2021, *ARA&A*, 653, A141
- Barrado y Navascués D., García López R. J., Severino G., Gomez M. T., 2001, *A&A*, 371, 652. doi:10.1051/0004-6361:20010409
- Barrado y Navascués D., Stauffer J. R., Jayawardhana R., 2004, *ApJ*, 614, 386
- Basri G., Marcy G. W., Graham J. R., 1996, *ApJ*, 458, 600
- Bergemann M., Gehren T., 2008, *A&A*, 492, 823
- Bergemann M., Kudritzki R.-P., Plez B., Davies B., Lind K., Gazak Z., 2012, *ApJ*, 751, 156
- Bergemann M., Kudritzki R.-P., Wurl M., Plez B., Davies B., Gazak Z., 2013, *ApJ*, 764, 115
- Bergemann M., Kudritzki R.-P., Gazak Z., Davies B., Plez B., 2015, *ApJ*, 804, 113
- Bertelli Motta C. et al., 2018, *MNRAS*, 478, 425
- Boesgaard A. M., Friel E. D., 1990, *ApJ*, 351, 467
- Bovy J., 2016, *ApJ*, 817, 49
- Bowen I. S., Vaughan A. H., 1973, *Applied Optics*, 12, 1430
- Campello, R. J. G. B., Moulavi, D., & Sander, J. 2013, *Advances in Knowledge Discovery and Data Mining*, ed.127 J. Pei, V. S. Tseng, L. Cao, H. Motoda, & G. Xu (Berlin, 128 Heidelberg: Springer Berlin Heidelberg), 160-172
- Casamiquela L., Castro-Ginard A., Anders F., Soubiran C., 2021, *A&A*, 654, A151. doi:10.1051/0004-6361/202141779
- Castelli F., Kurucz R. L., 2003, *IAUS*, 210, A20. doi:10.48550/arXiv.astro-ph/0405087
- Chambers K. C. et al., 2016, preprint (arXiv:1612.05560)
- Choi J. et al., 2016, *ApJ*, 823, 102
- Cunha K., Frinchaboy P. M., Souto D., Thompson B., Zasowski G., Allende Prieto C., Carrera R., et al., 2016, *AN*, 337, 922. doi:10.1002/asna.201612398

- Cutri R. M. et al., 2003, *2MASS All Sky Catalog of Point Sources*, 2246
- Cutri R. M. et al., 2014, *VizieR Online Data Catalog*: II/328
- Dahm S. E., 2015, *ApJ*, 813, 108
- De Silva G. M. et al., 2015, *MNRAS*, 449, 2604
- De Silva G. M., Sneden C., Paulson D. B., Asplund M., Bland-Hawthorn J., Bessell M. S., Freeman K. C., 2006, *AJ*, 131, 455
- De Silva G. M., Freeman K. C., Asplund M., Bland-Hawthorn J., Bessell M. S., Collet R., 2007, *AJ*, 133, 1161
- Donor J. et al., 2020, *ApJS*, 159, 199
- Dotter A., 2016, *ApJS*, 222, 8
- Dotter A., Conroy C., Cargile P., Asplund M., 2017, *ApJ*, 840, 99
- El-Badry, K., Ting, Y.-S., Rix, H.-W., et al. 2018, *MNRAS*, 476, 528. doi:10.1093/mnras/sty240
- Ester, M., Kriegel, H.-P., Sander, J., & Xu, X. 1996, *Proceedings of the Second International Conference on 135 Knowledge Discovery and Data Mining, KDD'96 (AAAI136 Press)*, 226-231
- Feng Y., Krumholz M. R., 2014, *Nature*, 513, 523
- Foreman-Mackey D., Hogg D. W., Lang D., Goodman J., 2013, *PASP*, 125, 306. doi:10.1086/670067
- Frinchaboy P. M., Thompson B., Jackson K. M., O'Connell J., Meyer B., Zsawski G., Majewski S. R., et al., 2013, *ApJL*, 777, L1. doi:10.1088/2041-8205/777/1/L1
- Funayama H., Itoh Y., Oasa Y., Toyota E., Hashimoto O., Mukai T., 2009, *PASJ*, 61, 931
- Gaia Collaboration, 2018, *A&A*, 616, A10
- Gaia Collaboration, Brown A. G. A., Vallenari A., Prusti T., de Bruijne J. H. J., Babusiaux C., Biermann M., et al., 2021, *A&A*, 649, A1. doi:10.1051/0004-6361/202039657
- García Pérez A. E. et al., 2016, *AJ*, 151, 144
- Gao X. et al., 2018, *MNRAS*, 481, 2666
- Gavel A., Gruyters P., Heiter U., Korn A. J., Nordlander T., Scheutwinkel K. H., Richard O. A., 2021, *A&A*, 652, A75
- Gebran M., Monier R., 2008, *A&A*, 483, 567
- Goodman J., Weare J., 2010, *CAMCOS*, 5, 65. doi:10.2140/camcos.2010.5.65
- Gossage S., Conroy C., Dotter A., Choi J., Rosenfield P., Cargile P., Dolphin A., 2018, *ApJ*, 863, 67
- Gruyters P., Korn A. J., Richard O., Grundahl F., Collet R., Mashonkina L. I., Osorio Y., Barklem P. S., 2013, *A&A*, 555, A31
- Gruyters P., Nordlander T., Korn A. J., 2014, *A&A*, 567, A72
- Gruyters P. et al., 2016, *A&A*, 589, A61
- Gunn J. E. et al., 2006, *AJ*, 131, 2332
- Gustafsson B. et al., 2008, *A&A*, 486, 951
- Holtzman J. A. et al., 2018, *AJ*, 156, 125
- Hui-Bon-Hoa A., Alecian G., 1998, *A&A*, 332, 224
- Hunt, E. L. & Reffert, S. 2021, *A&A*, 646, A104. doi:10.1051/0004-6361/202039341
- Hunt E. L., Reffert S., 2023, *A&A*, 673, A114. doi:10.1051/0004-6361/202346285
- Jofre ' P., Heiter U., Soubiran C., 2019, *ARA&A*, 57, 571
- Jönsson H. et al., 2020, *AJ*, 160, 120
- King J. R., Soderblom D. R., Fischer D., Jones B. F., 2000, *ApJ*, 533, 944
- Kollmeier, J. et al., 2019, *BAAS*, 51, 7
- Lawrence A. et al., 2007, *MNRAS*, 379, 1599
- Lind K., Korn A. J., Barklem P. S., Grundahl F., 2008, *A&A*, 490, 777
- Loaiza-Tacuri V., Cunha K., Souto D., Smith V. V., Guérco R., Chiappini C., Sales-Silva J. V., et al., 2023, *MNRAS*, 526, 2378. doi:10.1093/mnras/stad2896
- Lodieu N., P´erez-Garrido A., Smart R. L., Silvotti R., 2019, *A&A*, 628, A66
- Kaiser N. et al., 2002, in Tyson J. A., Wolff S. eds, *Proc. SPIE Conf. Ser. Vol. 4836, Survey and Other Telescope Technologies and Discoveries*. SPIE, Bellingham, p. 154
- Korn A. J., Grundahl F., Richard O., Mashonkina L., Barklem P. S., Collet R., Gustafsson B., Piskunov N., 2007, *ApJ*, 671, 402
- Krumholz M. R., McKee C. F., Bland-Hawthorn J., 2019, *ARA&A*, 57, 227
- Magrini L., Viscasillas Vázquez C., Spina L., Randich S., Romano D., Franciosini E., Recio-Blanco A., et al., 2023, *A&A*, 669, A119. doi:10.1051/0004-6361/202244957
- Majewski S. R. et al., 2017, *AJ*, 154, 94
- Martin A. J., Stift M. J., Fossati L., Bagnulo S., Scalia C., Leone F., Smalley B., 2017, *MNRAS*, 466, 613
- Masseron T., Merle T., Hawkins K., 2016, *BACCHUS: Brussels Automatic Code for Characterizing High accUracY Spectra*, ascl: 1605.004
- Mazzei P., Pigatto L., 1989, *A&A*, 213, L1
- Melo E., Souto D., Cunha K., Smith V. V., Wanderley F., Grilo V., Camara D., et al., 2024, arXiv, arXiv:2406.00111. doi:10.48550/arXiv.2406.00111
- Mermilliod J. C., 1981, *A&A*, 97, 235
- Michaud G., Alecian G., Richer J., 2015, *Atomic Diffusion in Stars, Astronomy and Astrophysics Library* (Cham: Springer)
- Myers N. et al., 2022, *AJ*, 164, 85
- Nidever D. L. et al., 2015, *AJ*, 150, 173
- Nordlander T., Gruyters P., Richard O., Korn A. J., 2024, *MNRAS*, 527, 12120
- Nordlander T., Korn A. J., Richard O., Lind K., 2012, *ApJ*, 753, 48
- O'Dell M. A., Hendry M. A., Collier Cameron A., 1994, *MNRAS*, 268, 181
- Osorio Y., Allende Prieto C., Hubeny I., Mészáros S., Shetrone M., 2020, *A&A*, 637, A80. doi:10.1051/0004-6361/201937054
- Plez B., 2012, *Turbospectrum: Code for spectral synthesis*, ascl, 1205.004, 616, A3
- Prša A. et al., 2016, *AJ*, 152, 41
- Semenova E. et al., 2020, *A&A*, 643, A164
- Shetrone M., Bizyaev D., Lawler J. E., Allende Prieto C., Johnson J. A., Smith V. V., Cunha K., et al., 2015, *ApJS*, 221, 24. doi:10.1088/0067-0049/221/2/24
- Skrutskie M. F. et al., 2006, *AJ*, 131, 1163
- Smith V. V. et al., 2013, *ApJ*, 765, 16
- Smith V. V. et al., 2021, *AJ*, 161, 254
- Sneden C., Bean J., Ivans I., Lucatello S., Sobeck J., 2012, ascl.soft. ascl:1202.009
- Soderblom D. R., Laskar T., Valenti J. A., Stauffer J. R., Rebull L. M., 2009, *AJ*, 138, 1292
- Souto D. et al., 2016, *ApJ*, 830, 35
- Souto D. et al., 2018, *ApJ*, 857, 14
- Souto D. et al., 2019, *ApJ*, 874, 97
- Souto D. et al., 2020, *ApJ*, 890, 133
- Souto D. et al., 2021, *ApJ*, 917, 11
- Souto D. et al., 2022, *ApJ*, 927, 123
- Spina L., Meléndez J., Casey A. R., Karakas A. I., Tucci-Maia M., 2018, *ApJ*, 863, 179
- Spina L., Magrini L., Cunha K., 2022, *Univ.*, 8, 87. doi:10.3390/universe8020087
- Stauffer J. R., Schultz G., Kirkpatrick J. D. 1998, *ApJ*, 499, 199
- Stauffer J. R. et al., 2007, *ApJS*, 172, 663
- Takeda Y., Hashimoto O., Honda S., 2016, *PASJ*, 69, 1
- Thoul A. A., Bahcall J. N., Loeb A., 1994, *ApJ*, 421, 828
- Vandenberg D. A., Bridges T. J., 1984, *ApJ*, 278, 679
- van Leeuwen F., 2009, *A&A*, 497, 209
- Vauclair G., Vauclair S., Michaud G., 1978, *ApJ*, 223, 920
- Virtanen P., Gommers R., Oliphant T. E., Haberland M., Reddy T., Cournapeau D., Burovski E., et al., 2020, *NatMe*, 17, 261. doi:10.1038/s41592-019-0686-2
- Wanderley F., Cunha K., Souto D., Smith V. V., Cao L., Pinsonneault M., Allende Prieto C., et al., 2023, *ApJ*, 951, 90. doi:10.3847/1538-4357/acd4bd
- Wanderley F., Cunha K., Kochukhov O., Smith V. V., Souto D., Cao L., Covey K., et al., 2024, arXiv, arXiv:2406.13757. doi:10.48550/arXiv.2406.13757
- Wang S., Chen X., 2019, *ApJ*, 877, 116
- Wright E. L. et al., 2010, *AJ*, 140, 1868
- Wilson J. C. et al., 2010, *Proc. SPIE*, 7735, 77351C
- Wilson J. C. et al., 2019, *PASP*, 131, 055001

APPENDIX A: SPECTRAL LINES ADOPTED OR REMOVED FROM THIS WORK

Table A1: Adopted and Unadopted Lines

Element	Adopted Lines (Å)	Excluded Lines (Å)
Fe I	15395.1	15207.5
	15588.1	15245.0
	15592.2	15294.6
	15604.2	15335.2
	15621.7	15501.1
	15632.1	15662.0
	15686.3	15677.5
	15691.9	15723.6
	15904.4	15774.1
	15920.7	15868.6
	15967.7	15892.6
	16006.8	15911.3
	16071.5	15964.9
	16175.0	15980.7
	16179.5	16037.8
	16180.9	16040.7
	16185.9	16042.7
	16195.1	16075.9
	16204.2	16125.9
	16207.7	16165.0
	16213.5	16231.7
	16225.6	16517.2
	16284.8	16524.5
	16316.4	16561.8
	16394.4	16645.9
	16398.2	
	16486.6	
	16522.1	
	16541.6	
	16665.5	
	16753.1	
C I	15784.7	16004.9
		16021.7
Na I	16373.9	
	16388.9	
Mg I	15879.5	15740.7
	15886.2	15749.0
	15954.5	15765.8
Al I	16763.4	16719.0
		16750.6
Si I	15361.2	15888.4
	15376.8	15960.1
	16215.7	16060.0
	16680.8	16094.8
	16828.2	
K I	15163.1	
	15168.4	
Ca I	16136.8	
	16150.8	
	16155.2	
	16157.4	
Ti I	15602.8	15334.8
	15699.0	15543.8
	16635.2	15715.6
V I	15924.0	
Cr I	15680.1	
Mn I	15159.0	15217.0
	15262.0	